이학석사 학위논문

Highly siderophile element geochemistry and Os isotopes of the Kalaymyo ophiolite, Myanmar: Exploring the influence of partial melting and mantle-melt interaction

미얀마 깔레이미요 오피올라이트의 친철성 원소 및 Os 동위원소 지구화학: 부분용융과 맨틀-용융체 상호반응의 영향

August 2023

서울대학교 대학원

지구환경과학부

김 봉 주

Highly siderophile element geochemistry and Os isotopes of the Kalaymyo ophiolite, Myanmar: Exploring the influence of partial melting and mantle-melt interaction

지도 교수 박 정 우

이 논문을 이학석사 학위논문으로 제출함
2023년 5월

서울대학교 대학원
지구환경과학부
김 봉 주

김봉주의 이학석사 학위논문을 인준함
2023년 7월

Chair	이 상 묵	(Seal)
Vice Chair	박 정 우	(Seal)
Examiner	이 현 우	(Seal)

Abstract

The understanding of the effect of partial melting and mantle-melt interaction on the geochemistry of highly siderophile elements (HSEs) in the upper mantle remains limited. To shed light on this matter, this study focuses on investigating the HSE geochemistry and Os isotopes of the Kalaymyo ophiolitic peridotite. Previous research has identified two distinct groups within the peridotite based on petrography and geochemistry. Group 1 samples exhibit low spinel Cr# along with high whole-rock Al_2O_3 and CaO contents, indicating that they represent residual mantle peridotite after a small degree of partial melting. On the other hand, Group 2 samples display higher spinel Cr# and lower whole-rock Al_2O_3 and CaO contents compared to Group 1, suggesting a higher degree of partial melting. Moreover, Group 2 samples show various mantle-melt interaction textures and higher spinel TiO_2 contents. These intriguing set of features presented by the Kalaymyo ophiolitic peridotite provide an excellent opportunity for us to explore and analyze the effects of partial melting and mantle-melt interaction on the HSE and Os isotopic compositions of the upper mantle peridotite in greater detail.

The whole-rock HSE contents are not significantly affected by the serpentinization process. The concentrations of iridium-group platinum group elements (IPGEs) increase with the degree of partial melting. According to the near-fractional dynamic melting model, olivine emerges as the dominant host phase for IPGEs after sulfide exhaustion. The significant differences observed in duplicate analyses suggest that IPGE-rich phases also play an important role in controlling the IPGE concentrations in highly depleted harzburgites, which is consistent with the presence of IPGE-rich platinum group minerals in the harzburgite.

On the other hand, the concentrations of palladium-group platinum group

elements (PPGEs) in Group 1 samples remain constant or slightly decrease with increasing degrees of partial melting, while Group 2 samples display more significant variations. Peridotite samples with the lowest PPGE contents at a given Al_2O_3 could be indicative of variations caused by partial melting. These trend are best explained by the sulfide exhaustion model with a lower bulk partition coefficient of PPGEs in comparison to that of IPGEs. The role of residual silicate and oxide minerals in controlling PPGE geochemistry is thought to be limited.

In Group 2 samples, the primary sulfides are almost exhausted, as indicated by the melting model. We suggest the higher Pd and Pt contents, along with elevated Pd/Ir ratios, in some Group 2 samples compared to the partial melting model can be accounted for by the addition of PPGE during mantle-melt interaction. This hypothesis is supported by the occurrence of Pd-bearing Cu-Ni alloy and Pt-Fe alloys associated with amphiboles and the sulfide addition model.

Rhenium behaves incompatibly during partial melting, showing progressive decrease in Re with decreasing Al_2O_3. Interestingly, Re is not significantly enriched during mantle-melt interaction and precipitation of secondary sulfides. This phenomenon is likely ascribed to the oxidizing conditions associated with subduction-related melt resulted, causing Re to behave as a lithophile element rather than being compatible to secondary sulfide phases.

The Os isotope ratios of the studied samples range from 0.1249 to 0.1286, except for one sample with a high value of 0.1331. The values are comparable to those of modern abyssal peridotites without significant seawater contamination.

Keyword: Highly siderophile and chalcophile elements, Partial melting, Mantle-melt interaction
Student Number: 2021-28917

Table of Contents

List of Tables

List of Figures

Chapter 1. Introduction

Partial melting and mantle-melt interaction are fundamental geological processes that the upper mantle experiences. The upper mantle becomes depleted in incompatible elements through partial melting, producing basaltic melts. The residual mantle may interact with various types of melts in the lithosphere, which modifies its geochemistry and mineralogy (Dijkstra et al., 2003). Understanding these geological processes is crucial for unraveling the heterogeneity of the upper mantle and the diversity of mantle-derived magmas.

While the behavior of lithophile elements during these processes is well-documented, that of highly siderophile elements (HSEs), including the platinum group elements (PGEs) and rhenium (Re), remains relatively poorly understood. HSEs are known to have chalcophile characteristics and are primarily hosted in sulfide phases in the upper mantle (Mithell and Keays, 1981). They are suggested to undergo fractionation during partial melting, although the exact process that results in the elemental fractionation remains debated. Previous studies have shown depletion in palladium-group PGEs (PPGEs; Rh, Pd, Pt) relative to iridium-group PGEs (IPGEs; Ru, Os, Ir) during partial melting (e.g., J. Liu et al., 2010; Pearson et al., 2004). Rhenium behaves similarly to PPGEs. The more compatible behavior of IPGEs compared to PPGEs and Re has been attributed to residual olivine and IPGE-bearing PGMs (platinum group metals) (Fonseca et al., 2012; Brenan et al., 2016). However, recent experimental studies suggested a wide variation in partition coefficients between sulfide melt and silicate melt ($D^{sulf/sil}$) for Pd, ranging from 2,000 to 536,000 (Mungall and Brenan, 2014; Zhang and Li, 2021), which requires further

investigation on the role of sulfide melts in HSE geochemistry during partial melting.

Additionally, the influence of melts produced by partial melting of the asthenospheric mantle on the sulfide and HSE compositions of the lithospheric mantle during upwelling remains to be investigated (Luguet and Reisberg, 2016). The percolation of S-undersaturated melt would lead to the dissolution of residual sulfides remaining after the partial melting event. The dissolution of sulfides would result in a significant depletion in HSE concentrations (e.g., Lorand et al. 2003; Liu et al. 2010;). Conversely, primary S-saturated melts produced by low degrees of partial melting or volatile-rich evolved melts derived from S-undersaturated melts would precipitate Cu-Ni-rich sulfides with elevated Pd contents (e.g., Lorand et al., 2004). The interaction involving slab derived melt and oxidizing fluids occurs in regions affected by subduction leading to preferential mobilization of Os and Pd over the other HSEs (Alard et al. 2011). Nevertheless, the specific conditions varying response to changes in pressure (P), oxygen fugacity (fO_2), and sulfide saturation and compositions of these melts are challenging to predict, thereby obscuring the precise effects of mantle-melt interaction.

In terms of the Os isotope system, the daughter isotope ^{187}Os behaves compatibly, whereas the parent isotope ^{187}Re behaves incompatibly in the mantle environment. This behavior distinguishes it from other isotope systems such as Rb-Sr, Sm-Nd, and U-Th-Pb where both daughter and parent isotopes behave incompatibly (Shirey and Walker, 1998). The different compatibility between Re and Os results in strong Re/Os fractionation, leading to distinctive isotopic signatures such as substantially unradiogenic Os isotopes in the residual mantle and radiogenic Os isotopes in the melts as they age. Because of the high Os contents in the residual lithospheric mantle, it is likely that the mantle records the initial melt depletion

events even after late-stage alteration and metasomatism (Walker et al., 1989). Therefore, Os isotopic systematics can serve as valuable indicators for ancient melting processes and provide insights into the geochemical evolution of mantle rocks.

The Kalaymyo ophiolitic peridotites have experienced various degrees of partial melting and mantle-melt interaction. Park et al. (2022) divided the peridotites into two groups according to petrographic observation and spinel composition. The Group 1 samples have low spinel Cr# (<0.3) and TiO_2 (<0.068 wt.%), representing residual mantle peridotite after a small degree of partial melting. In contrast, the Group 2 samples have higher spinel Cr# (>0.3) with varying TiO_2 contents (0.065-1.874 wt.%), showing that they underwent a higher degree of partial melting and varying mantle-melt interaction. The Group 2 samples have a moderately positive correlation between Cr# and TiO_2 of spinel, which indicates that the origin of the melt reacted with Group 2 samples is from the subduction zone. Therefore, the Kalaymyo ophiolitic peridotites provide an excellent opportunity to examine the effects of partial melting and mantle-melt interaction on the HSE and Os isotopic compositions of the upper mantle peridotite.

In this study, I present HSE abundances and Os isotopic compositions for a suite of peridotites from the Bophi-Vum region of the Kalaymyo ophiolite, Myanmar. The microscale characterization of platinum group minerals (PGMs) using an electron microprobe (EPMA) and Scanning Electron Microscope (SEM) was also carried out to constrain the host phases of HSEs.

Chapter 2. Geological background

The ophiolites in Myanmar are composed of two north-south-trending belts that are separated by the dextral strike-slip Sagaing fault zone (Fig. 1b). To the northeast of the fault zone, ophiolites extend from Myitkyina to the Yalung-Tsangpo suture (YZSZ), while in the southwest, they stretch from Manipur through Kalaymyo to Andaman Island. The northeast ophiolites are estimated to have formed within the time range of approximately 166-176 Ma, whereas the southwest ophiolites are reported to have formed around 125 Ma (Yang et al., 2012; Liu et al., 2016a). It is suggested that the older northeast ophiolites originated from the Meso-Tethys Ocean, while the southwest ophiolites are associated with the Neo-Tethys Ocean (Liu et al., 2016a).

The southwest ophiolites spanning the Indo-Burma Range exhibit diverse geological characteristics. The Manipur ophiolite, located in the northern part of the southwest ophiolites, is predominantly characterized by abyssal peridotites based on mineralogical and geochemical analyses (Singh, 2013), whereas the Andaman ophiolite in the southern region is believed to have formed in supra-subduction environments (Ghosh et al., 2014). The Kalaymyo ophiolite, located in the central part of the India-Burma Range, displays characteristics of both mid-ocean ridge (MOR) type and supra-subduction zone (SSZ) type ophiolites (Liu et al., 2016b; Niu et al., 2018; Park et al., 2022). This suggests that a variety of oceanic lithospheric rocks have been juxtaposed during the process of obduction in this region.

The western part of the India-Burma Range, where the Kalaymyo ophiolite is located, is composed of Cretaceous to Eocene sedimentary rocks, while the eastern

part consists of Triassic pelites and turbidites (Mitchell, 1981). The Kalaymyo ophiolite is thrust over the western side of the India-Burma Range (Fig. 1c).

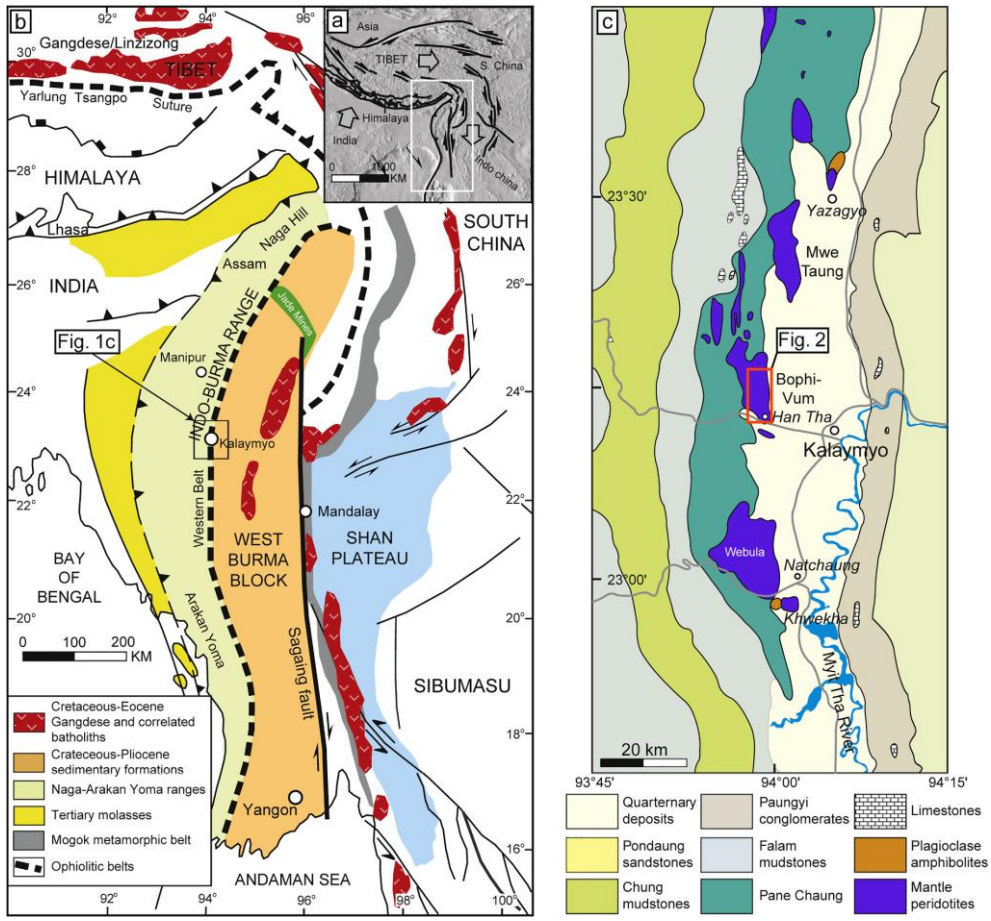

Figure 1. (a) Outline of tectonic settings of Myanmar from Liu et al., (2016b). (b) A geological map of Myanmar from Park et al., (2022). (c) A detailed view of the regional geology surrounding the Kalaymyo ophiolite, from Park et al., (2022).

Chapter 3. Samples and Methods

3.1. Sample selection

Outcrop and core samples were collected from the exploration area (12 km^2) in Kalaymyo based on preliminary investigations conducted by the Korea Institute of Geoscience and Mineral Resources (KIGAM) and the Department of Geological Survey and Exploration (DGSE) in Myanmar. From the collected samples, a careful selection process was employed to choose representative peridotites for the purposes of this study. Twelve Kalaymyo peridotite samples reported by Park et al. (2022) were selected for this study, and their respective sampling locations are provided in Table 1 and depicted in Fig. 2. Among these samples, six samples are Group 1 samples with varying degrees of partial melting, and the other six are Group 2 samples with higher degrees of partial melting and a wide range of mantle-melt interaction. The Group 1 samples exhibit Cr# of 0.14-0.22 and demonstrate a negative correlation between Cr# and TiO_2 content in spinel, following the trend of fractional melting of depleted mid-ocean ridge mantle (Fig. 3). On the other hand, the Group 2 samples display Cr# ranging from 0.31 to 0.68 with a positive correlation between Cr# and TiO_2 content in spinel (Fig. 3).

Table 1. Whole-rock major element contents [wt.%] of the mantle peridotite

Sample		Group 1						Group 2					
		DKR1165	DKR1166	DKR1289	BDH-06	BDH-03(71)	BDC-15/01	BDH-13(m,25.2-.3)	BDH-12	BDH05_2(F)	BDH-05(e,15.6-.7)	BDC-5/10	BDH-18
Type		Outcrop	Outcrop	Outcrop	Borehole	Borehole	Borehole	Borehole	Borehole	Borehole	Borehole	Borehole	Borehole
UTM (46Q)	x	600214	600264	600414	601425	601693	601734	601195	601609	601359	601359	601262	601257
	y	2573573	2573574	2573675	2572875	2571119	2569807	2571412	2571146	2572409	2572409	2570968	2572807
Core depth [m]	Top				94.1	71	24.1	25.2	12.7	15.95	15.6	24.5	9.85
	Bottom				94.2	71.2	25.1	25.3	12.8	16.05	15.7	25.6	10
Reference		This study			Park et al. (2022)			Park et al. (2022)		This study	Park et al. (2022)		
Alteration level*		2	2	3	1	1	1	1	2	2	1	3	1
SiO_2		45.0	45.0	42.3	45.4	44.0	45.8	45.1	43.8	41.4	44.6	45.4	45.5
MgO		34.9	39.3	35.9	40.4	42.1	40.8	42.4	44.2	44.1	44.4	43.6	43.7
FeO_{tot}		8.69	9.04	9.35	7.71	8.14	8.06	7.84	8.39	8.37	7.62	8.21	8.33
Al_2O_3		3.58	2.64	2.22	2.00	1.55	1.89	1.54	1.12	0.93	1.24	0.85	0.55
CaO		3.14	1.92	2.48	2.40	2.07	2.11	1.82	1.19	0.54	0.96	0.66	0.66
TiO_2		0.07	0.05	0.05	0.08	0.06	0.03	0.02	0.01	0.01	0.02	0.01	0.01
MnO		0.14	0.14	0.13	0.13	0.13	0.14	0.13	0.13	0.13	0.13	0.13	0.14
Na_2O		0.06	0.04	0.04	0.12	0.10	0.19	0.22	0.19	0.03	0.18	0.20	0.18
K_2O		0.02	0.02	0.02	0.01	0.01	0.01	0.01	0.01	0.01	0.01	0.01	0.01
P_2O_5		0.01	0.01	0.01	0.02	0.02	0.01	0.01	0.01	0.01	0.01	0.01	0.01
LOI		3.88	1.57	7.10	2.33	1.94	4.63	3.40	1.77	4.00	4.82	10.21	4.78
Total		99.5	99.7	99.6	98.3	98.2	99.1	99.1	99.1	99.5	99.1	99.0	99.1

*degree of alteration under the microscope and hand specimen as well as LOI; (1) only tiny portion of alteration mineral can be found; (2) each grain has intact portion more than 50% in average; (3) each grain has intact portion but less than 50%; (4) Whole rock is composed of bastite, serpentine and iddingsite

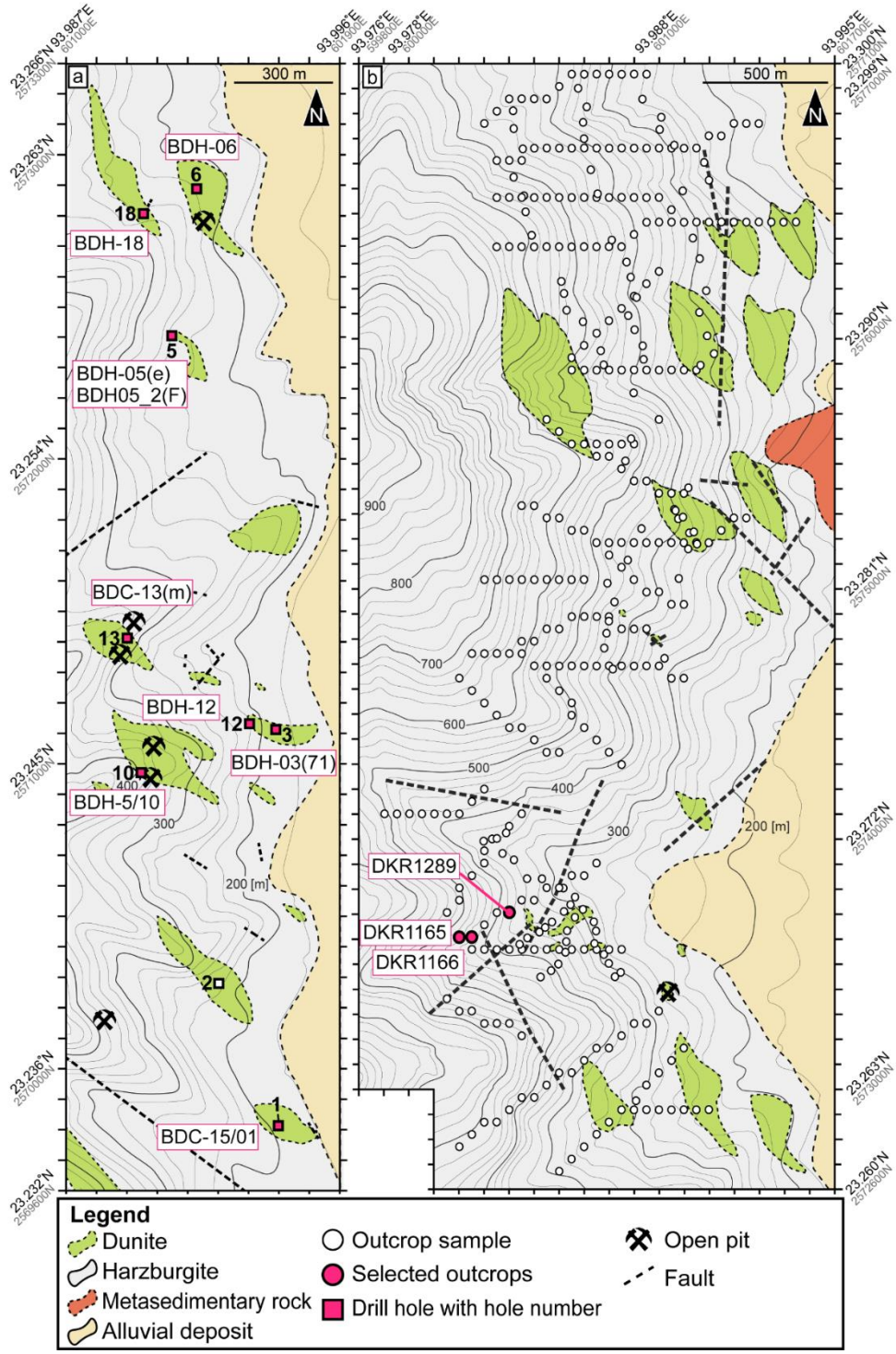

Figure 2. Geological maps showing (a) the locations of drill sites in the southern region of the study area, and (b) the collection points of outcrop samples within the northern sector of the study area, modified from Park et al., (2022).

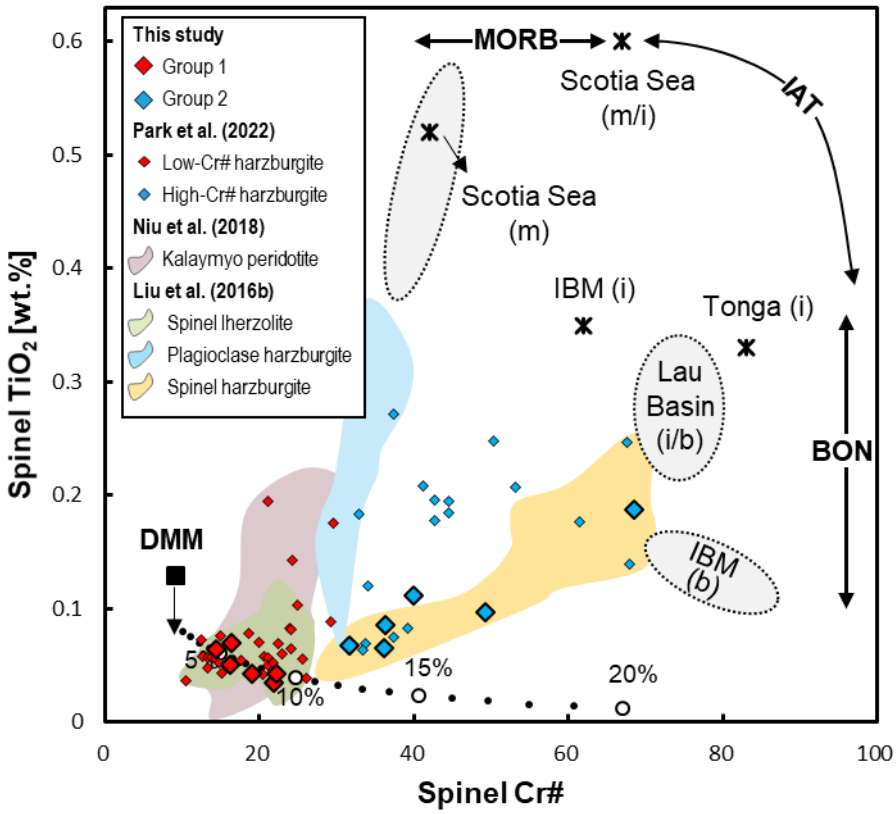

Figure 3. Comparison of TiO_2 composition and Cr# for Cr-spinel, modified from Park et al. (2022). Smaller diamonds represent the dataset from Park et al. (2022). Included in the graph are the TiO_2 composition and Cr# of spinel from several sources: East Scotia Sea basalts (Saunders and Tarney, 1979), Lau-Tonga arc basalts (Allan, 1994; Sobolev and Danyushevsky, 1994), island arc tholeiites, and boninites from the Izu-Bonin-Mariana system (van der Laan et al., 1992). The reference-derived trend for each tectonic setting is also displayed (Pearce et al., 2000). Chemical affinity for each spinel is marked as follows: 'm' for mid-ocean ridge, 'i' for island-arc, and 'b' for boninite. The dotted line demonstrates a model of Cr# and TiO_2 composition of spinel based on fractional partial melting of the mantle source, where TiO_2 composition of spinel is slightly lower than in the depleted MORB mantle (Workman and Hart, 2005). Small open circles along the curved line represent the Cr# and TiO_2 composition of spinel corresponding to specific degrees of partial melting.

3.2. Whole Rock Major and Trace Element Analysis

Whole-rock major oxide concentrations were determined by a Shimadzu XRF-1700 instrument at NCIRF (National Center for Inter-university Research Facilities at SNU) using fused glass disks. The analytical uncertainties of the XRF data at NCIRF were estimated by multiple analyses of the reference peridotites MUH-1 during each analysis. The outcrop samples (DKR1165, DKR1166, DKR1289) and one core sample (BDH05_2(F)) were analyzed in this study, while the remaining samples were sourced from Park et al. (2022). The major elements data (> 1 wt%), such as SiO_2, Al_2O_3, FeO, MgO, and CaO, show percent differences of <2.8% compared to the reported values.

Whole-rock trace elements were determined by laser-ablated inductively coupled plasma mass spectrometry (LA–ICP–MS) at the Korea Institute of Ocean Science and Technology (KIOST), consisting of a 193 nm excimer LA system (ESI NWR 193) coupled to an Agilent 7700 quadrupole ICP–MS. Data reduction was performed with an iolite program based on the methodology of Paton et al. (2011). The analyzed isotopes are ^{27}Al, ^{29}Si, ^{43}Ca, ^{47}Ti, ^{51}V, ^{53}Cr, ^{55}Mn, ^{57}Fe, ^{59}Co, ^{61}Ni, ^{65}Cu, ^{66}Zn, ^{71}Ga, ^{85}Rb, ^{85}Rb, ^{88}Sr, ^{89}Y, ^{90}Zr, ^{93}Nb, ^{133}Cs, ^{137}Ba, ^{139}La, ^{140}Ce, ^{141}Pr, ^{146}Nd, ^{147}Sm, ^{153}Eu, ^{157}Gd, ^{159}Tb, ^{163}Dy, ^{165}Ho, ^{166}Er, ^{169}Tm, ^{175}Yb, ^{175}Lu, ^{178}Hf, ^{181}Ta, ^{208}Pb, ^{232}Th, and ^{238}U, where ^{29}Si is the internal standard in this study. The analyses were conducted at a laser pulse rate of 7 Hz, an energy intensity of ~3 J/cm^2, and a beam size of 150 μm. A BCR-2g glass was analyzed together in order to monitor the precision and reproducibility of the analyses. A NIST612 reference material was used as a primary standard. The accuracy monitored with MUH-1, BCR-2g was

generally smaller than 15 %.

3.3. Whole-rock HSE Analysis

The whole-rock HSE contents of the Myanmar peridotite samples were determined using a Ni-sulfide fire assay – isotope dilution technique described by Park et al. (2012). Prior to analysis, the surface of rock chips was ground to remove surface alteration and contamination. Three grams of powdered sample were mixed with Na-borax (3 g), Ni (0.3 g), and S (0.15 g) in an inner crucible. A mixed spike solution containing HSE (^{99}Ru, ^{105}Pd, ^{185}Re, ^{191}Ir, and ^{195}Pt) was added to the mixture. The inner crucible was then placed in an outer crucible containing 0.5 g of flour. The mixtures were dried at 100°C for 60 minutes in a furnace and then fused at 1200°C for 20 minutes. Nitrogen gas was injected into the furnace during fusion to create a reducing environment. After the fusion, the crucible was removed and subsequently quenched. The nickel sulfide beads were separated from the quenched glass, dissolved in 175 ml of 6 N HCl at 160°C, and then filtered through a Millipore filter paper. The solution was completely digested in 4 ml of aqua regia, and the matrix was changed into 5 ml of 2% HCl, which was refluxed at 100°C for 2 hours. The final solution was analyzed by Agilent 8900 quadrupole ICP-MS, and the HSE contents of the peridotites were calculated using the isotope dilution technique.

Procedural blanks were determined by conducting sample-free analyses using 6 g of sodium borax, 0.3 g of Ni, and 0.15 g of S for each session. The accuracy and precision of the analytical method were assessed through replicate analysis of the international standard MUH-1 (harzburgite). Procedural blanks for the method and

HSE analyses of MUH-1 are provided in Table A1. The obtained procedural blanks were subtracted from the data. The reproducibility of MUH-1 analyses is approximately <20%, and the results are consistent with the preferred data of standard samples (Meisel, personal communication).

3.4. Whole-rock Re-Os isotope system Analysis

The Re-Os concentration and Os isotope composition were determined for 12 samples by high-pressure asher (HPA-S) combined with the isotope dilution method. 3 g of sample powder was put into a 50 ml Teflon-sealed quartz glass tube together with the mixed PGE spiked solution (enriched in ^{99}Ru, ^{108}Pd, ^{185}Re, ^{190}Os, ^{191}Ir, and ^{198}Pt). Spiked sample powder was digested in 5 ml of distilled HNO_3 and 3 ml distilled HCl mixture at 300 °C and 100 bar for 3 h using HPA-S. The solutions were recovered and transferred into the PFA vials for the determination of Os concentration and Os isotope compositions while the residues were kept for the Re concentration measurement.

During digestion, Os is oxidized in the form of OsO_4, which is volatile while oxides of other elements are not. Thus, only OsO_4 is easily purged by directing the carrier gas into the PFA vials containing the sample solutions, following the method of Hassler et al. (2000) and Meisel et al. (2001). The OsO_4 signals were directly obtained by introducing the carrier gas directly into Agilent 7500 ICP-MS at the University of Leoben. For each sample, the carrier Ar gas flow rate was optimized for the highest Os signal intensity. ^{186}Os, ^{187}Os, ^{188}Os, ^{189}Os, ^{190}Os, and ^{192}Os signals were measured while ^{185}Re and ^{193}Ir signals were monitored together for the undesired introduction of a solutions droplet by too strong bubbling.

The mass fractionation and instrumental drift were externally corrected by bracketing each sample with DROsS, Os isotope standard material (Luguet et al., 2008). The corrected $^{192}Os/^{188}Os$ ratio was used to determine the Os concentration based on the isotope dilution method assuming the natural abundance of ^{192}Os and ^{188}Os of samples. To obtain a true $^{187}Os/^{188}Os$ ratio of the sample, the mixing curve between the sample and spike was assumed. On the diagram of $^{187}Os/^{188}Os$ versus $^{190}Os/^{188}Os$, based on the curve calculated using the spike information and measured data, a true $^{187}Os/^{188}Os$ was obtained assuming the natural abundance of ^{190}Os and ^{188}Os of samples. After Os isotope measurements, the sample solution was combined with the residue again.

Only supernatant was collected in the PFA vial, the same one used for Os isotope measurement, and evaporated overnight on the hot plate. The sludge was dissolved into 10 ml of 0.8 M HNO_3 and it is used for Re separation. Biorad 2 ml disposable columns, which were soaked in 1:1 diluted HNO_3 heated up to 65 °C and rinsed three times with deionized water, were used. They were filled with 2 ml of pre-cleaned anion exchange resin AG1x8 (100-200 mesh in MQ). Before loading the samples, the resin-filled columns were rinsed and conditioned with H_2O, 6 N M HNO_3, and 0.8 M HNO_3. After sample loading, the columns are rinsed sequentially with 10 mL of 1 M HCl and 20 mL of 0.8 M HNO_3. Re was collected in 10 ml of 6 N HNO_3 by eluting 12 ml of 6 N HNO_3. The solution was dried down overnight and re-dissolved into 2 % HNO_3, which is used for Re concentration measurement conducted by Agilent 8800 ICP-MS at the University of Leoben. The mass fractionation was externally corrected by bracketing each sample with Re standard solution. The Re concentrations were calculated by the isotope dilution method using ratios of corrected counts rates of $^{185}Re/^{187}Re$. The Os and Re concentration and

$^{187}Os/^{188}Os$ of a reference material, MUH-1 (Montauniversität Harzburgite) are consistent with the reported values (Snortum and Day, 2020) within one sigma (Table A1).

3.5. Mineral Chemical Analysis

The major element concentrations of olivine, orthopyroxene, and clinopyroxene from selected samples were analyzed by a semiquantitative method using Oxford instruments X-max 50mm energy-dispersive silicon drift detectors (EDS) attached to JSM-7100F at the School of Earth and Environment Sciences, SNU. The analysis was performed using a 10 mm working distance, with a process time of 5, a probe current of 11 nA, and an accelerating voltage of 15 kV. I acquired 1,000,000 counts for each data point, which corresponds to an acquisition time of approximately 60 seconds. Prior to each analysis session, I conducted energy calibration and beam measurement using the JEOL cobalt standard. This calibration process used a process time of 6 and 2,000,000 acquisition counts, corresponding to an acquisition time of approximately 120 seconds. The compositions of the spinels are from Park et al. (2022). The compositions of the spinel grains are sourced from Park et al. (2022). The compositions of amphibole grains in Group 2 samples were determined using an electron probe micro-analysis (EPMA) at NCIRF, utilizing the same analytical conditions as the spinel analysis.

To ensure the accuracy and precision of and EDS analyses, I monitored the compositions of three reference minerals (NMMNH111312-44 olivine, NMNH117733 diopside, and NMNH117075 chromite) in each session. The major

element compositions of olivine show a relative percent difference of less than 3.1% compared to reported values, with a relative standard deviation of less than 0.7%. The minor elements NiO (~0.43 wt.%) and MnO (~0.16 wt.%) exhibit slightly higher relative standard deviations of about 13% and 15%, respectively. For the diopside, the major element compositions show a relative percent difference of less than 1.7% compared to the working standard value (n=29), with a relative standard deviation of less than 0.6%. However, the minor elements Al_2O_3 (~0.26 wt.%) and FeO_{tot} (~0.25 wt.%) show slightly higher relative standard deviations of about 21% and 14%, respectively. The major element compositions of chromite show a relative percent difference of less than 2.0% compared to the reported values, with a relative standard deviation of less than 0.8%. The minor elements TiO_2 (~0.12 wt.%) and MnO (~0.22 wt.%) exhibit slightly higher relative standard deviations of about 16% and 31%, respectively. I calculated the ferrous-to-ferric iron ratio of spinel based on theoretical spinel stoichiometry ($X^{2+}Y_2^{3+}O_4$) following the method described in Park et al. (2012).

3.6. PGM analysis

PGM (platinum group minerals) analysis was conducted on polished thin sections using a high-resolution JEOL JSM-7100F field emission scanning electron microscope (FE-SEM) at the School of Earth and Environmental Sciences, SNU. The analysis was performed at an acceleration voltage of 20 kV, a probe current of 11nA, and a working distance of 10 mm to qualitatively identify PGMs in the backscattered mode. The brightness threshold of the backscattered electron image

was adjusted to highlight particles with similar characteristics to sulfides and PGMs, enabling the distribution of high atomic weight particles to be examined. Quantitative analysis was not possible due to the small sizes of the PGMs (1-8 μm). The major components of platinum group elements were confirmed through EDS spectra.

Chapter 4. Results

4.1. Petrography

The fresh part of the Kalaymyo peridotties used in this study is composed of olivine (67-85 vol%), orthopyroxene (11-28 vol%), clinopyroxene (1.4-5.9 vol%), spinel (~1 vol%) with traces of sulfide and PGMs (Fig. 4, 5). They have undergone varying serpentinization degrees, which replaced the primary mantle minerals with secondary minerals such as serpentine and magnetite.

A comprehensive examination of the petrography of the peridotites is presented in Park et al. (2022). Below is a summary of their findings. Peridotites are protogranular to porphyroclastic (Fig. 4a, b). Group 1 samples are composed of lherzolites and harzburgites and exhibit vermicular to lobate-shaped spinel associated with pyroxene (Fig. 4c). In contrast, Group 2 samples are composed of harzburgites and have granular or polygonal-shaped spinel closely associated with olivine (Fig. 4d). Olivine ovoidal inclusion and embayment texture are also observed in Group 2 samples (Fig. 4e, f). The peridotites are penetrated by serpentine veins in company with magnetite, with silicate minerals demonstrating serpentinization from rim to core. The majority of samples contain only tiny amounts of alteration minerals, or their grains have an intact portion of over 50% on average. However, DKR1289 and BDC-5/10 display a wide range of alteration, with an intact portion of less than 50%.

Sulfide and alloy grains in Kalaymyo peridotites occur as inclusions to mainly interstitial and intergranular forms (Fig. 5, 6), with sizes varying from a few μm to

hundreds of μm. Sulfides are predominantly composed of Fe-Ni sulfide and pyrrhotite aggregate rimmed by awaruite ($Ni_{2-3}Fe$, Fig. 5a). Group 1 samples have sulfide and alloy inclusions in silicate minerals (Fig 5b). In BDH-13(m) of Group 2 sample, interstitial sulfide associated with amphibole is observed within the cleavage of clinopyroxene (Fig. 5c), and Cu-rich alloy can be seen inside amphibole penetrating clinopyroxene (Fig. 5d).

Platinum group mineral (PGM) grains were identified in the studied thin section of Group 2 samples via SEM, namely IPGE, Ir-Pt, and Pt-Fe alloy. (Fig. 6). The IPGE-rich alloy, with a major and minor axis of ~8 and ~3 μm respectively, is attached to the rim of intergranular sulfide (Fig. 6e). This alloy is associated with a sub-grain that is an Ir-Pt alloy. The host sulfide comprises of pyrrhotite rimmed by magnetite. Within the pyrrhotite, prismatic pentlandite exsoulution and Fe-Co alloy are grown.

The Pt-Fe alloy, presenting a ~1 μm square shape (Fig. 6g), was found as an inclusion within paragasitic amphibole (Fig. 6f) that penetrate along the cleavage of the primary clinopyroxene. Additional minerals, including awaruite, pentlandite, and a Pd-rich Cu alloy, were observed at the outer edge of the paragasitic amphibole.

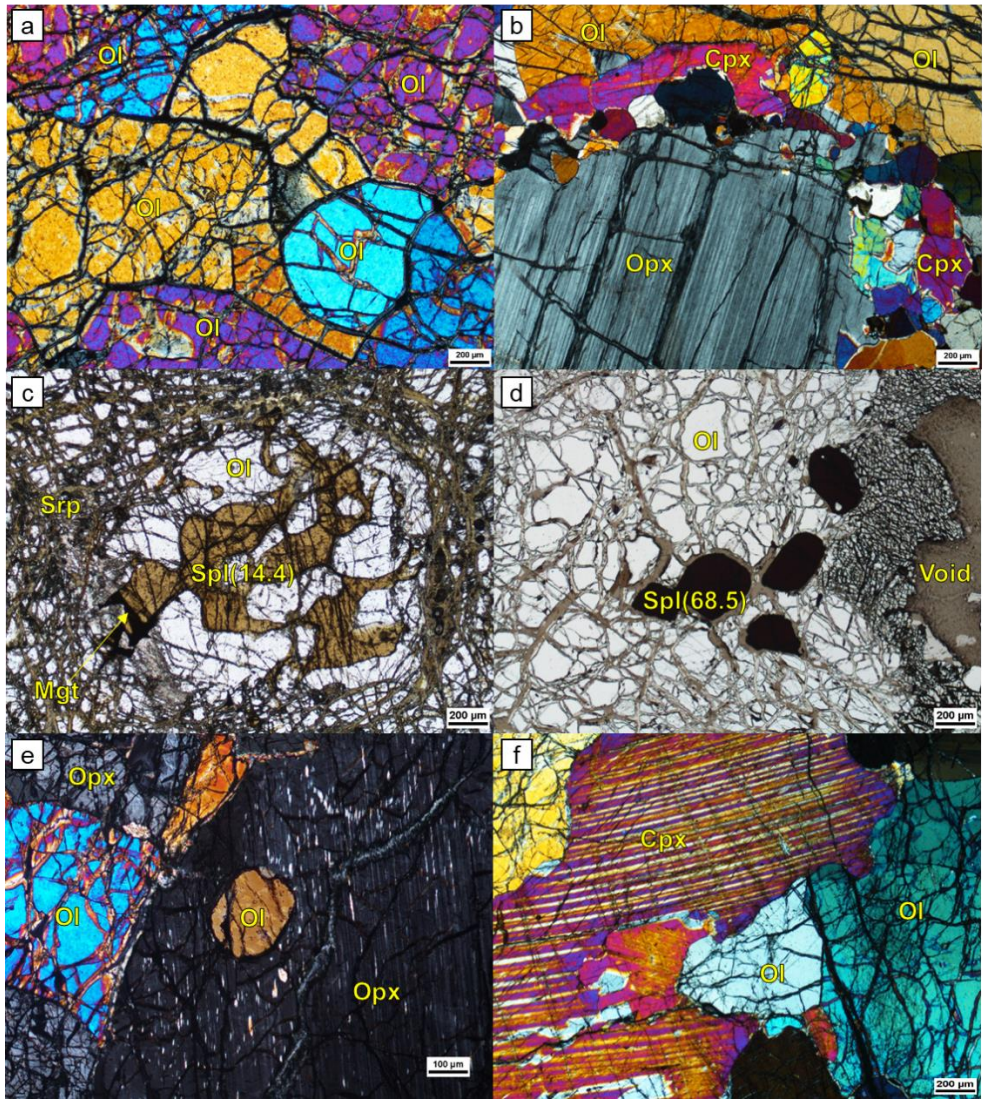

Figure 4. Microstructures of Kalaymyo peridotites. (a) Protogranular texture. (b) Orthopyroxene porphyroclast enclosed within neoblastic olivine and clinopyroxene. (c) spinel with a symplectitic shape in olivine with serpentine mesh. (d) Euhedral spinel with olivine. (e) Olivine ovoidal inclusion in orthopyroxene. (f) Clinopyroxene with orthopyroxene exsolution lamellae and olivine embayment Ol: olivine, Opx: orthopyroxene, Cpx: clinopyroxene, Srp: serpentine, Mgt: magnetite, Spl: spinel, Brackets = spinel Cr#.

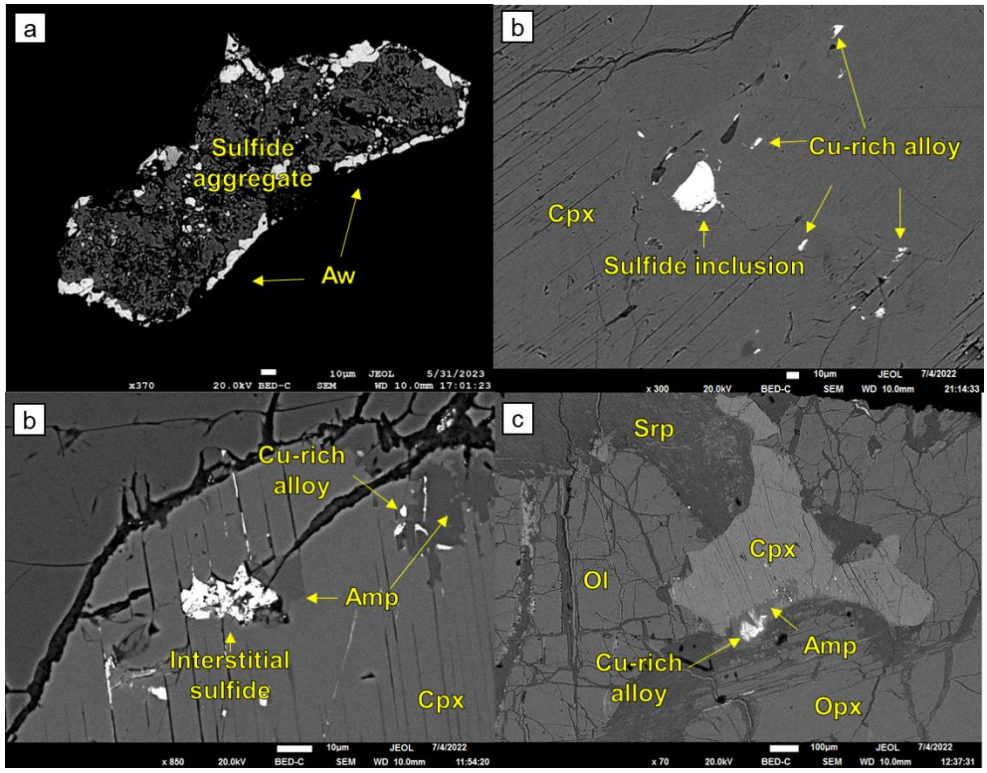

Figure 5. Backscattered Electron (BSE) images of base metal sulfides (BMS) in Kalaymyo peridotites. (a) Intergranular sulfide aggregate rimmed by awaruite. (b) Sulfide inclusion in clinopyroxene with Cu-rich alloy (c) Interstitial sulfide associated with amphibole in the clinopyroxene cleavage. (d) Amphibole penetrating clinopyroxene with Cu-rich alloy. Aw: awaruite, Cpx: clinopyroxene, Amp: amphibole, Srp: serpentine, Ol: olivine, Opx: orthopyroxene**.**

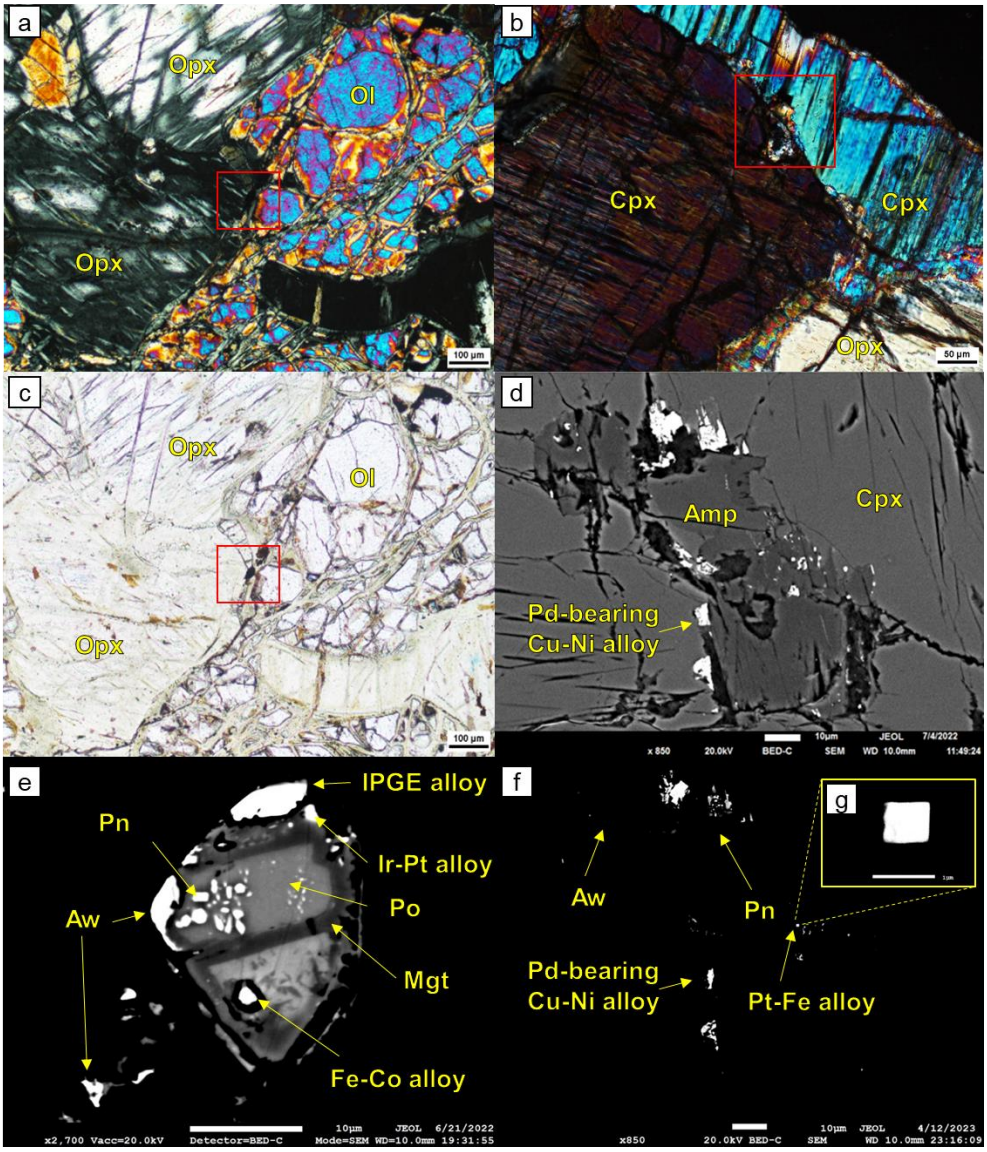

Figure 6. Microstructures of platinum-group minerals (PGM) in Kalaymyo peridotites. (a, c, e) Fe-Os-Ir-Ru alloy and associated textures, (b, d, f) Pt-Fe alloy and associated amphibole and clinopyroxene. (g) Magnified view of the Pt-Fe alloy shown in (f). Ol: olivine, Opx: orthopyroxene, Cpx: clinopyroxene, Amp: amphibole, Pn: pentlandite, Aw: awaruite, Po: pyrrhotite, Mgt: magnetite**.**

4.2. Whole-rock compositions

The major and trace element compositions of the Kalaymyo peridotites are presented in Tables 1 and 2. With the exception of samples DKR1289 and BDC-5/10, the majority of the samples show a moderate degree of serpentinization, as indicated by low values of loss on ignition (LOI) ranging from 1.57-4.78 wt.%. DKR1289 and BDC-5/10 are representative of serpentinized peridotites, displaying higher LOI values of 7.10 and 10.2 wt.%, respectively. In the Al_2O_3/SiO_2 versus MgO/SiO_2 diagram (Fig. 8b), most of the analyzed peridotites plot near the terrestrial array (Zindler and Hart, 1986; Jagoutz et al., 1979).

Group 1 and Group 2 samples exhibit distinct variations in major element compositions. Group 1 samples display less refractory compositions, characterized by low MgO contents ranging from 34.9-42.1 wt.% and high contents of SiO_2 (42.3-45.8 wt.%), TiO_2 (0.03-0.08 wt.%), FeO_{tot} (7.71-9.35 wt.%), CaO (1.92-3.14 wt.%), and Al_2O_3 (1.55-3.58 wt.%). In contrast, Group 2 samples exhibit more refractory compositions with higher MgO contents ranging from 42.4-44.4 wt.% and lower contents of SiO_2 (41.4-45.5 wt.%), Al_2O_3 (0.55-3.58 wt.%), TiO_2 (0.01-0.02 wt.%), FeO_{tot} (7.62-8.39 wt.%), and CaO (0.54-1.82 wt.%). The whole-rock concentrations of Group 1 samples predominantly included within the field of abyssal peridotites, while those of Group 2 samples plot within the SSZ peridotite field (Fig. 7). When plotted on the anhydrous Al_2O_3 vs. MgO diagram (Fig. 8a), the Kalaymyo peridotites follow a trend consistent with residues after variable degrees of partial melting.

The Kalaymyo peridotites exhibit variable depletion patterns of chondrite-normalized rare earth elements (REEs) (Fig. 9). The whole-rock trace element

concentrations of the Kalaymyo peridotites are listed in Table 2. Lanthanum is not reported because its concentrations of standard material is significantly higher than the reported value. The Group 2 samples have a higher mean Ce/Nd ratio (1.20) than the Group 1 samples (0.95). The chondrite-normalized REE patterns of Group 1 samples are included in the area of the abyssal peridotites (Niu, 2004). The concentrations of REEs in the Kalaymyo peridotites show varying degrees of depletion, ranging from 4.1 to 22.5% relative to the depleted MORB mantle (DMM) in terms of heavy rare earth element (HREE) compositions.

Table 2. Whole-rock trace element contents [ppm] of the mantle peridotite

	Group 1						Group 2					
Sample	DKR1165	DKR1166	DKR1289	BDH-06	BDH-03(71)	BDC-15/01	BDH-13(m,25.2-.3)	BDH-12	BDH05_2(F)	BDH-05(e,15.6-.7)	BDC-5/10	BDH-18
Type	Outcrop	Outcrop	Outcrop	Borehole	Borehole	Borehole	Borehole	Borehole	Borehole	Borehole	Borehole	Borehole
Ti	478.5	366.0	360.9	310.6	192.1	222.6	100.8	157.0	115.5	167.2	98.5	120.9
V	96.2	62.2	65.7	70.5	61.2	63.1	41.9	47.8	28.9	40.0	36.8	42.7
Cr	3877.8	2477.4	2788.1	2917.1	2402.1	2965.5	2508.7	2724.5	2506.2	2666.3	2933.0	2905.0
Mn	1067.0	983.4	1063.7	1079.9	1100.9	1069.8	987.9	1066.5	950.2	1026.3	1087.0	1105.9
Fe	23299.5	24811.2	23770.8	27654.6	23536.7	22951.4	22191.8	23214.3	22067.3	22213.7	30088.9	23506.8
Co	101.1	103.5	108.6	110.0	116.5	115.0	111.6	122.8	114.5	114.7	121.4	112.9
Ni	3089.6	3708.4	3450.3	2149.2	2293.4	2350.7	2262.4	2477.3	2432.4	2353.5	2445.9	2183.4
Cu	30.4	31.5	25.6	28.7	19.4	35.7	17.8	16.4	11.5	5.1	7.2	9.3
Zn	53.1	42.5	41.3	42.0	43.1	39.4	37.0	36.6	37.1	33.0	42.3	37.9
Ga	3.6	2.1	2.6	2.2	1.9	2.1	1.2	1.6	1.1	1.2	1.1	0.9
Sr	0.680	0.899	0.742	0.948	0.721	0.556	0.142	0.603	0.683	0.216	0.649	0.391
Y	2.313	1.674	1.330	1.331	0.990	0.962	0.334	0.605	0.278	0.429	0.269	0.210
Zr	0.781	0.848	0.699	0.614	0.453	0.475	0.339	0.410	0.570	0.465	0.465	0.328
Ce	0.029	0.029	0.023	0.053	0.058	0.054	0.007	0.025	0.077	0.016	0.072	0.009
Pr	0.011	0.015	0.007	0.007	0.008	0.007	0.002	0.004	0.009	0.003	0.008	0.002
Nd	0.113	0.125	0.072	0.045	0.029	0.031	0.012	0.026	0.040	0.020	0.036	bdl
Sm	0.115	0.086	0.060	0.039	0.027	0.028	0.012	0.019	0.017	0.014	0.016	0.006
Gd	0.206	0.152	0.119	0.101	0.065	0.074	0.024	0.045	0.024	0.027	0.021	0.009
Tb	0.044	0.037	0.025	0.026	0.020	0.018	0.007	0.013	0.005	0.009	0.006	0.004
Dy	0.372	0.260	0.198	0.196	0.148	0.153	0.048	0.092	0.042	0.053	0.035	0.028
Ho	0.088	0.063	0.052	0.049	0.037	0.037	0.015	0.024	0.012	0.015	0.009	0.008
Er	0.276	0.204	0.172	0.162	0.133	0.125	0.044	0.081	0.040	0.059	0.038	0.029
Yb	0.304	0.215	0.189	0.192	0.154	0.159	0.072	0.100	0.061	0.093	0.053	0.043
Lu	0.047	0.034	0.033	0.032	0.027	0.025	0.011	0.019	0.010	0.015	0.010	0.007
Hf	0.060	0.046	0.039	0.030	0.022	0.020	0.010	0.018	0.021	0.019	0.014	0.008
Ta	0.060	0.060	0.060	0.008	0.007	0.005	0.005	0.006	0.061	0.006	0.008	0.006
Th	0.002	0.003	0.002	0.009	0.008	0.017	0.003	0.009	0.011	0.004	0.018	0.003
U	0.002	0.007	0.003	0.006	0.004	0.004	0.003	0.003	0.004	0.002	0.004	0.002

(bdl - below detection limit)

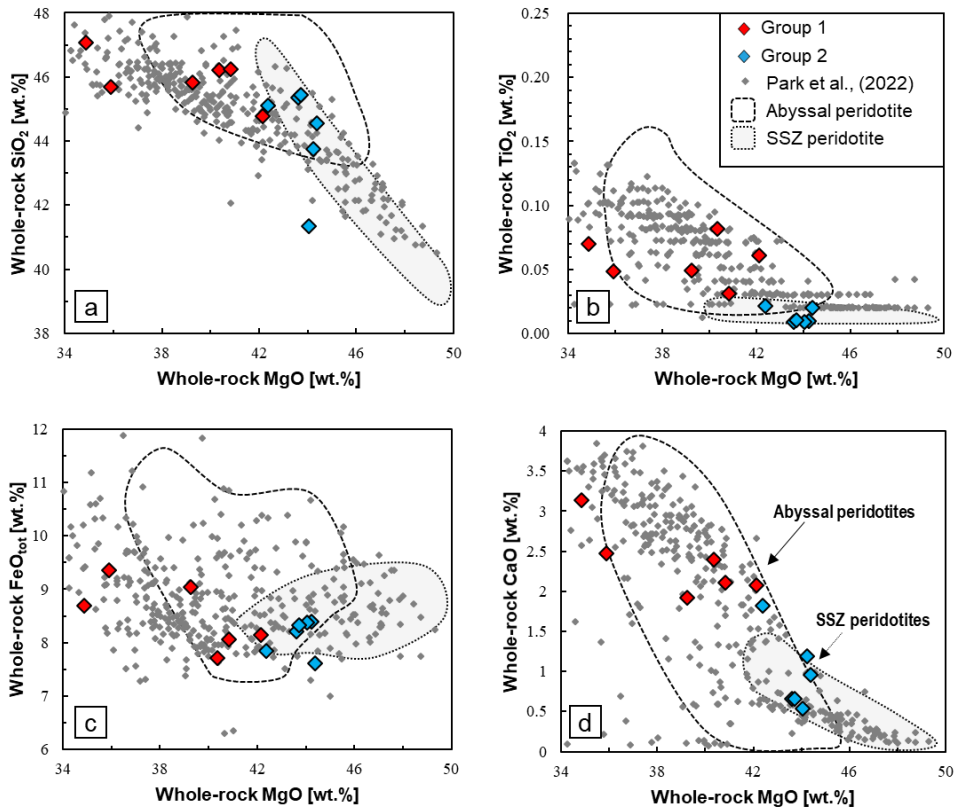

Figure 7. Harker diagrams showing whole-rock major oxide compositions of Kalaymyo peridotites against whole-rock MgO contents (wt.%). Small grey diamonds are data from Park et al., (2022). Supra-subduction zone (SSZ) and abyssal peridotite fields are from Parkinson and Pearce (1998) and Niu et al., (1997), respectively.

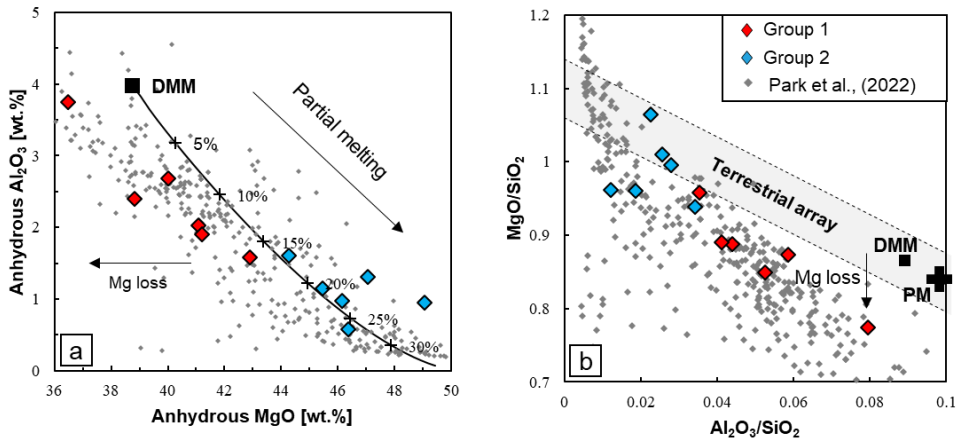

Figure 8. Whole-rock major element data of Kalaymyo peridotites. Small grey diamonds are data from Park et al., (2022). (a) Plot of bulk-rock anhydrous Al_2O_3 vs. MgO. The melting curves from the depleted MORB mantle (DMM, Workman and Hart, 2005) are calculated using the model of Niu (1997). (b) Plot of bulk-rock MgO/SiO_2 vs. Al_2O_3/SiO_2. The grey area in Fig. 8(b) is the 'Terrestrial array' (Zindler and Hart, 1986). The arrow with Mg loss indicate the effect of serpentinization. Compositions of DMM and primitive mantle (PM, McDonough and Sun, 1995) are shown for comparison.

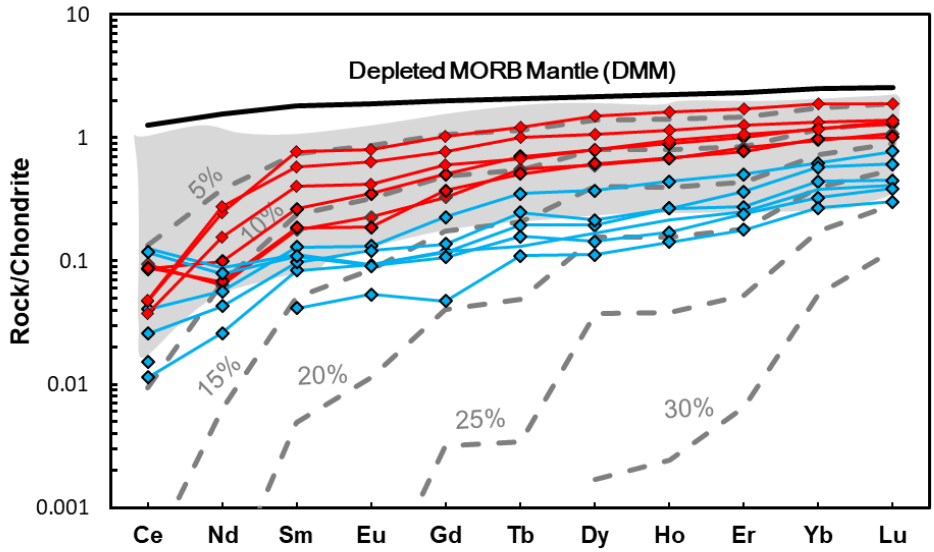

Figure 9. Whole-rock REE composition of the Kalaymyo peridotites normalized to chondrite (McDonough and Sun, 1995) and non-modal fractional melting model from a DMM (Salters and Stracke, 2004). Equations are derived from Johnson et al. (1990). The grey dashed lines are modeled peridotite compositions after 5%, 10%, 15%, 20%, 25%, and 30% partial melting. The grey area indicates the compositional range of abyssal peridotites, as presented by Niu (2004).

4.3. Whole Rock HSE and Os isotopic compositions

The whole-rock concentrations of HSE and Os isotopic ratios in the Kalaymyo peridotites are presented in Table 3. Group 1 samples exhibit HSE contents ranging from 3.25-5.90 ppb for Os, 3.20-4.59 ppb for Ir, 5.91-8.47 ppb for Ru, 1.11-1.45 ppb for Rh, 6.62-8.59 ppb for Pt, 6.13-8.59 ppb for Pd, and 0.17-0.35 ppb for Re. The HSE concentrations in Group 1 samples are generally similar to those of primitive upper mantle (PUM), with the exception of one sample, DKR1289 (Fig. 10a). DKR1289 stands out with lower Pd (4.94 and 4.75 ppb) and Re (0.063 and 0.069 ppb) values compared to other Group 1 samples. As the whole-rock Al_2O_3 content increases, IPGE and Rh concentrations increase, while Pd and Pt concentrations remain constant or slightly decrease (Fig. 11). On the other hand, Group 2 samples display a wider range of HSE concentrations, ranging from 2.30-8.52 ppb for Os, 2.89-6.17 ppb for Ir, 4.98-11.12 ppb for Ru, 0.95-1.73 ppb for Rh, 5.46-12.94 ppb for Pt, 3.09-7.43 ppb for Pd, and 0.01-0.21 ppb for Re, exhibiting a more diverse pattern compared to Group 1 (Fig. 10b). It should also be noted that several Group 2 samples (BDH-05(e,15.6-.7), BDC-5/10, BDH-18) show significant differences in HSE concentrations between duplicate analyses (Fig. 11). In terms of inter-correlation between HSEs, Ir shows positive correlations with Os and Ru, to a certain extent with Rh and Pt. However, a broad negative correlation is observed between Ir and Re (Fig. 12). Palladium does not exhibit any significant inter-correlation with other HSEs (Fig. 12e).

The whole-rock $^{187}Os/^{188}Os$ ratios of the Kalaymyo peridotites generally exhibit subchondritic values ranging from 0.1239 to 0.1286, with the exception of one

sample, DKR1165, which displays a suprachondritic ratio of 0.1331 (Fig. 13). This range is consistent with the isotopic composition of residual peridotites. However, no correlation is observed between the whole-rock isotopic ratio and whole-rock $^{187}Re/^{188}Os$, Al_2O_3 content, or Cr# of spinel (Fig. 13).

Table 3. Whole-rock HSE [ppb] and Os isotope compositions of the mantle peridotite

Sample	Group	Os	Ir	Ru	Rh	Pt	Pd	Re	ΣPGE	Pd/Ir	$^{187}Re/^{188}Os$	$^{187}Os/^{188}Os$	2σ
DKR1165	Group 1	3.3	3.2	5.9	1.1	6.6	6.7	0.201	26.82	2.09	0.2530	0.1331	0.0032
Duplicate		3.4	3.4	6.4	1.2	7.4	6.7	-	28.48	1.98			
DKR1166		5.4	4.7	7.5	1.2	7.7	4.9	0.063	31.45	1.06	0.8556	0.1259	0.0025
Duplicate		4.9	4.5	7.5	1.2	7.5	4.8	0.069	30.31	1.07			
DKR1289		4.6	4.0	7.7	1.5	7.5	7.2	0.203	32.46	1.78	0.2450	0.1239	0.0034
Duplicate		4.9	4.3	8.0	1.4	8.3	7.2	0.177	34.15	1.70			
BDH-06		5.0	3.9	6.8	1.3	7.4	6.6	0.244	31.09	1.69	0.3248	0.1263	0.0016
Duplicate		4.5	3.6	6.3	1.3	7.1	6.2	0.258	29.13	1.73			
BDH-03(71)		3.9	3.7	6.7	1.2	6.2	6.1	0.297	27.78	1.66	0.4987	0.1275	0.0014
Duplicate		4.4	3.4	6.5	1.2	6.2	6.2	0.352	27.89	1.83			
BDC-15/01		5.1	4.3	7.8	1.4	8.3	6.4	0.180	33.35	1.49	0.2708	0.1274	0.0012
Duplicate		5.9	4.6	8.5	1.4	8.6	6.7	0.247	35.76	1.47			
BDH-13(m,25.2-.3)	Group 2	5.4	4.1	7.1	1.1	7.1	5.9	0.204	30.61	1.45	0.1734	0.1249	0.0029
Duplicate		5.1	3.5	6.5	1.0	7.0	6.3	0.121	29.49	1.78			
BDH-12		4.1	3.2	6.1	1.0	6.4	5.2	0.182	25.98	1.60	0.3248	0.1286	0.0021
Duplicate		4.2	3.5	6.0	1.0	6.7	5.0	0.211	26.31	1.45			
BDH05_2(F)		4.2	3.8	7.1	1.4	6.8	8.0	0.045	31.32	2.12	0.0907	0.1253	0.0023
Duplicate		4.0	3.9	7.3	1.3	6.5	7.4	0.050	30.42	1.90			
BDH-05(e,15.6-.7)		6.5	5.0	8.3	1.8	7.8	3.4	0.019	32.77	0.68	0.0454	0.1252	0.0011
Duplicate		8.5	6.2	11.1	1.7	9.8	3.8	0.008	41.10	0.61			
BDC-5/10		2.3	2.9	5.0	1.1	5.9	3.1	n.d.	20.26	1.07	0.0792	0.1258	0.0023
Duplicate		3.8	4.4	7.0	1.5	5.5	3.3	0.014	25.47	0.75			
BDH-18		4.6	4.9	7.4	1.6	12.9	6.1	0.010	37.46	1.24	0.0367	0.1268	0.0017
Duplicate		4.9	4.3	6.7	1.2	10.8	7.2	0.010	35.09	1.67			

2σ = 2 standard deviation

n.d. = not determined

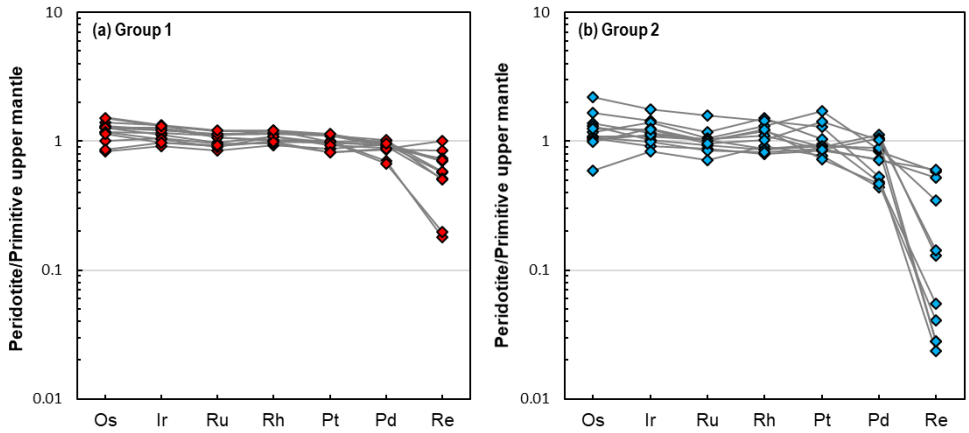

Figure 10. Primitive mantle normalized PGE patterns for (a) Group 1 and (b) Group 2 samples. Normalizing values after Becker et al., (2006).

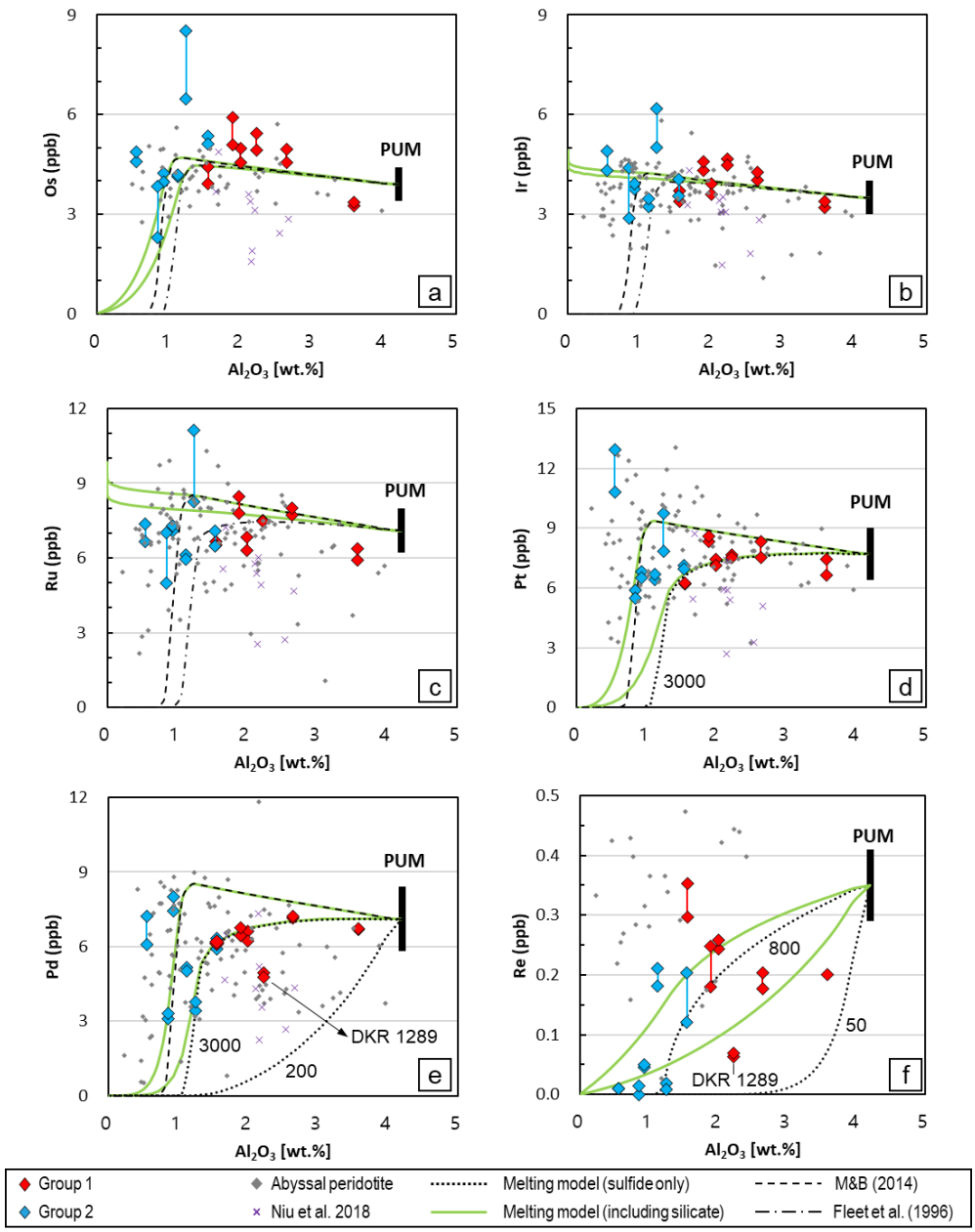

Figure 11. Variations of HSE with respect to whole-rock Al_2O_3 contents in peridotites (Black column: Primitive Mantle from Becker et al., 2006). The grey diamonds are compiled data of abyssal peridotite from Barnes et al. (2015). The purple x marks are data of the Kalaymyo peridotite from Niu et al. (2018). Lines are the near-fractional melting models assuming fractionation resulting from partitioning between sulfide liquid and silicate melt. The green line is a melting model which includes partition coefficients between silicate mineral and silicate melt ($D^{sil.min/sil.melt}$). The dashed and dash-dotted line is based on partition coefficients between sulfide melt and silicate melt ($D^{sulf/sil}$) from Mungall and Brenan (2014) and Fleet et al. (1996), respectively. Numbers on figures are $D^{sulf/sil}$ used for the melting model. The partition coefficient values and references used in models are presented in Table 9.

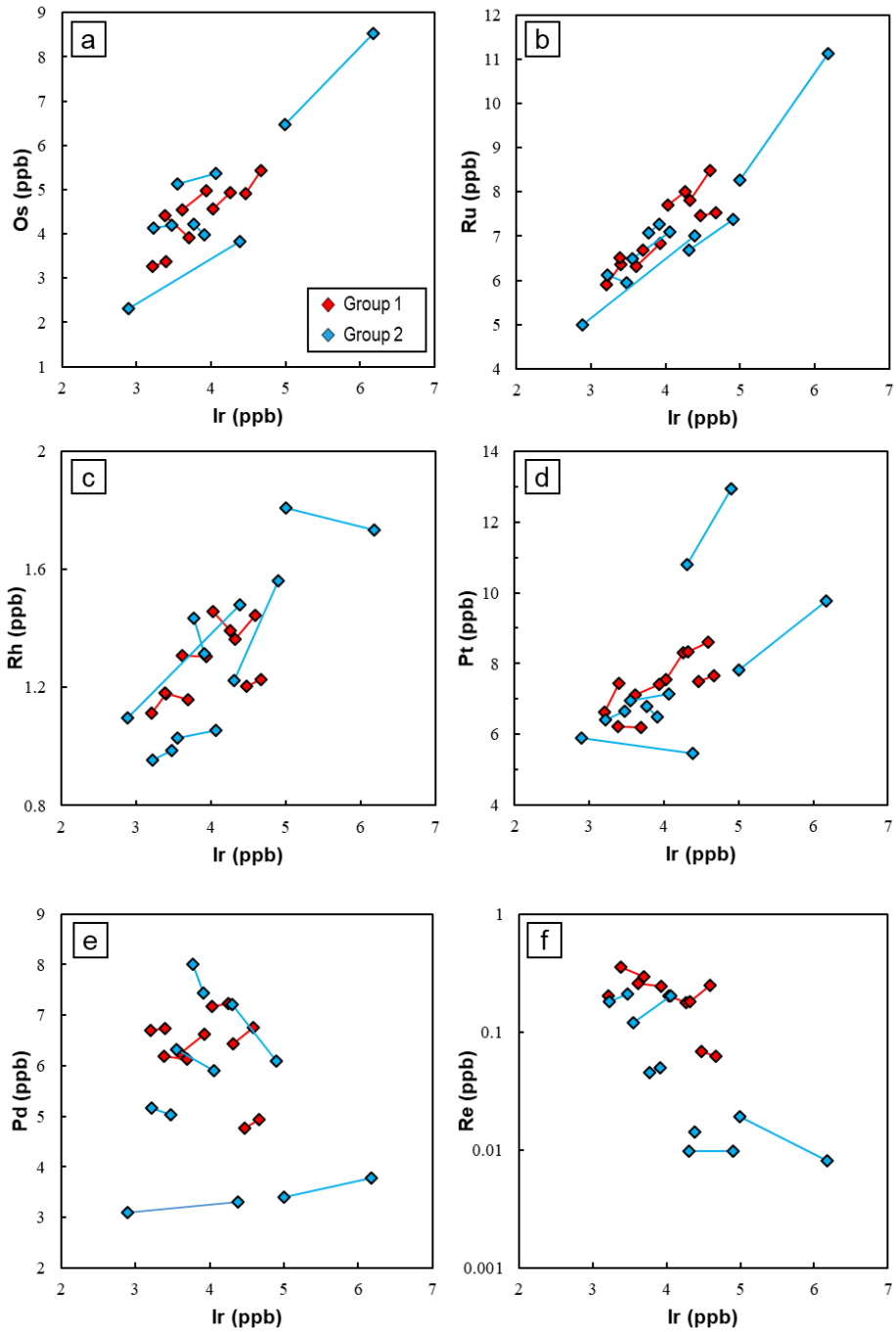

Figure 12. Covariation of the concentrations (in ppb) of Os, Ru, Rh, Pt, Pd, and Re with Ir for Kalaymyo peridotites.

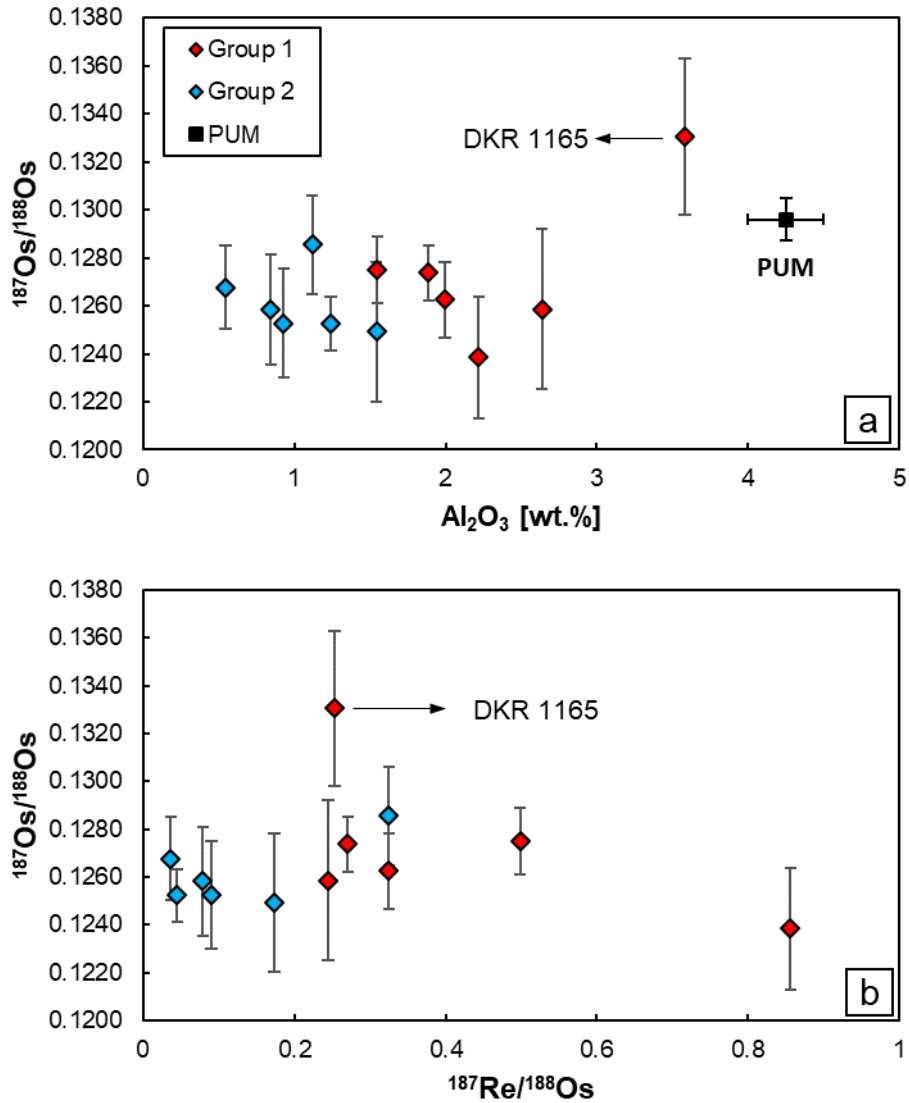

Figure 13. Variations of Os isotopes with respect to (a) whole-rock Al_2O_3 contents and (b) Re/Os in peridotites (Black cross mark: Primitive Upper Mantle from Meisel et al., 2001).

4.4. Mineral compositions

The compositions of selected spinel grains in the Kalaymyo peridotites from Park et al. (2022) are supplied in Table 4. Spinel grains from Group 1 samples exhibit Cr# values ranging from 0.14-0.22 and Mg# ratios of 0.72-0.76, with TiO_2 content below 0.069 wt.%. Spinel grains in Group 2 samples display comparable Cr# values ranging from 0.31-0.68 and Mg# ratios from 0.44 to 0.70, with TiO_2 content varying from 0.065 to 0.187.

The major element compositions of silicate minerals, including olivine, orthopyroxene, clinopyroxene, and amphibole, in the Kalaymyo peridotites are listed in Tables 5-9, respectively. Olivine grains in the Kalaymyo peridotites exhibit a narrower compositional range compared to other minerals. Their Fo numbers (Fo = molar Mg/(Mg+Fe)*100) range from 90.1-91.4, with MgO contents of 49.0-50.3 wt.% and FeO contents of 8.47-9.80 wt.%. The NiO and MnO values range from 0.36-0.46 wt.% and 0.11-0.17 wt.%, respectively. The compositions of olivine and spinel plot on the olivine-spinel mantle array (OSMA), with Group 1 and 2 samples aligning well with the area corresponding to abyssal and oceanic SSZ peridotites (Fig. 14).

The pyroxenes in the Kalaymyo peridotites show distinct compositions for each group. Orthopyroxenes in Group 1 samples have Mg# values of 89.9-90.5, Al_2O_3 contents of 3.13-4.23 wt.%, and Cr_2O_3 contents of 0.48-0.67 wt.%. In Group 2, orthopyroxenes display a compositional range with Mg# values of 90.8-94.0, Al_2O_3 contents of 1.18-3.67 wt.%, and Cr_2O_3 contents of 0.71-0.80 wt.%. Similarly, clinopyroxenes in Group 1 samples have Mg# values of 91.0-93.0, CaO contents of

21.9-23.5 wt.%, and Al_2O_3 contents of 3.60-5.66 wt.%. In Group 2, clinopyroxenes exhibit a compositional range with Mg# values of 92.3-94.0, CaO contents of 21.0-24.3 wt.%, and Al_2O_3 contents of 1.18-3.93 wt.%. Most of the pyroxenes in Group 1 and 2 samples plot within the areas corresponding to abyssal and SSZ peridotites, respectively (Fig. 15).

Amphiboles in the Kalaymyo peridotites are mostly paragasitic composition according to the classification diagram of Leake et al. (1997) (Fig. 16a). These amphiboles are specifically found in the Group 2 samples. These amphiboles are calcium-rich ($^{B}Ca/\Sigma B > 0.925$) and have Si contents ranging 6.2-6.5 apfu and (Na+K) contents of 0.59-0.66 apfu. They exhibit narrow ranges of Na_2O (2.00-2.40 wt.%), CaO (12.61-12.66 wt.%), and SiO_2 (44.18-46.43 wt.%), and their compositions plot within the areas corresponding to both suprasubduction and ophiolitic amphiboles (Fig. 16).

Platinum group minerals (PGMs) were identified in two Group 2 samples. BDH-13(m,25.2-3) contains Pt-Fe alloy and Pd-rich Cu-Ni alloy, while BDC-5/10 contains an IPGE alloy and an Ir-Pt subgrain together (Fig. 6). Quantitative analysis using electron microprobe was limited due to the small grain size of PGMs and their location within or in close proximity to silicates or base metal sulfides. Based on EDS spectra, the PGMs mainly consist of alloys such as Fe-Os-Ir-Ru alloy (IPGE alloy), Ir-Pt-rich alloy, Pt-Fe alloy, and Pd-rich Cu-Ni alloy (Fig. 17).

Table 4. Mean chromite compositions of selected mantle peridotite measured by electron probe micro-analyzer [wt.%]

Sample		Group 1						Group 2					
		DKR1165	DKR1166	DKR1289	BDH-06	BDH-03(71)	BDC-15/01	BDH-13(m)	BDH-12	BDH05_2(F)	BDH-05(e)	BDC-5/10	BDH-18
n		3	3	3	3	3	4	4	3	3	6	13	5
SiO_2	value	0.02	0.01	0.03	0.04	0.03	0.02	0.05	0.04	0.07	0.08	0.01	0.05
	1σ	0.01	0.01	0.01	0.02	0.02	0.00	0.01	0.01	0.03	0.02	0.02	0.02
TiO_2	value	0.06	0.05	0.07	0.04	0.03	0.04	0.07	0.07	0.09	0.11	0.10	0.19
	1σ	0.00	0.02	0.01	0.01	0.01	0.03	0.01	0.00	0.01	0.04	0.02	0.02
Al_2O_3	value	54.0	51.9	52.7	49.7	47.8	47.2	39.9	37.3	37.1	34.2	28.1	15.4
	1σ	2.3	0.3	0.5	0.5	0.6	1.9	0.5	0.5	1.1	0.6	0.5	0.9
Cr_2O_3	value	13.5	14.9	15.4	17.4	19.9	20.1	27.4	31.5	31.5	33.9	40.7	49.7
	1σ	2.5	0.8	0.6	0.8	0.5	2.2	0.5	0.4	0.8	1.5	0.8	1.1
FeO*	value	11.2	10.9	11.4	12.3	12.1	11.8	12.4	12.7	11.8	13.5	14.9	21.1
	1σ	0.3	0.2	0.1	0.4	0.8	0.7	1.2	0.4	1.2	0.9	0.7	1.0
Fe_2O_3*	value	0.9	1.0	0.8	1.6	1.0	2.4	2.4	2.0	1.6	1.8	1.6	3.4
	1σ	0.1	0.3	0.2	0.2	0.5	0.4	0.4	0.2	0.3	0.7	0.3	0.8
MnO	value	0.13	0.12	0.14	0.17	0.16	0.14	0.22	0.14	0.20	0.21	0.24	0.42
	1σ	0.02	0.03	0.01	0.01	0.03	0.03	0.01	0.03	0.01	0.02	0.02	0.03
MgO	value	18.7	18.4	18.5	17.7	17.4	17.8	16.6	16.4	16.8	15.4	13.8	8.1
	1σ	0.3	0.1	0.0	0.2	0.7	0.3	0.9	0.3	0.9	0.6	0.5	0.7
CaO	value	0.00	0.00	0.00	0.01	0.00	0.01	0.01	0.03	0.00	0.03	0.04	0.01
	1σ	0.00	0.00	0.00	0.02	0.00	0.00	0.01	0.01	0.00	0.04	0.05	0.01
NiO	value	0.34	0.31	0.30	n.d.	0.28	0.22	n.d.	n.d.	n.d.	n.d.	n.d.	n.d.
	1σ	0.02	0.02	0.03	-	0.08	0.06	-	-	-	-	-	-
Total		98.7	97.6	99.3	98.9	98.8	99.8	99.0	100.1	99.2	99.3	99.5	98.4
Mg#	value	74.9	75.0	74.2	71.9	71.9	72.8	70.4	69.8	71.7	66.9	62.3	40.7
	1σ	0.8	0.4	0.2	0.8	2.1	1.4	3.2	1.0	3.1	2.2	2.0	3.1
Cr#	value	14.4	16.2	16.4	19.0	21.8	22.2	31.6	36.2	36.3	39.9	49.3	68.5
	1σ	2.8	0.8	0.6	0.8	0.6	2.6	0.5	0.6	1.2	1.4	0.9	1.7

1σ = 1 sample standard deviation

n.d. = not determined

*ferric and ferrous iron content of spinel are calculated on the basis of stoichiometry

Table 5. Mean olivine compositions of mantle peridotite measured by EDS [wt.%]

		Group 1						Group 2					
Sample		DKR1165	DKR1166	DKR1289	BDH-06	BDH-03(71)	BDC-15/01	BDH-13(m)	BDH-12	BDH05_2(F)	BDH-05(e)	BDC-5/10	BDH-18
n		3	5	3	3	4	3	4	3	3	3	3	3
SiO_2	value	40.83	40.02	40.41	39.89	40.30	40.21	40.30	39.76	40.20	40.26	40.29	40.16
TiO_2	value	n.d.	n.d.	n.d.	n.d.	n.d.	n.d.	n.d.	n.d.	n.d.	n.d.	n.d.	n.d.
Al_2O_3	value	n.d.	n.d.	n.d.	n.d.	n.d.	n.d.	n.d.	n.d.	n.d.	n.d.	n.d.	n.d.
Cr_2O_3	value	n.d.	n.d.	n.d.	n.d.	n.d.	n.d.	n.d.	n.d.	n.d.	n.d.	n.d.	n.d.
FeO_{tot}	value	9.80	9.38	9.49	9.76	9.11	9.27	8.50	8.99	8.47	8.47	8.78	8.93
MnO	value	0.16	0.14	0.15	0.13	0.14	0.14	0.13	0.15	0.17	0.14	0.11	0.14
MgO	value	50.0	49.0	49.6	48.6	49.3	49.6	50.2	49.5	50.3	50.1	49.9	49.9
CaO	value	n.d.	n.d.	n.d.	n.d.	n.d.	n.d.	n.d.	n.d.	n.d.	n.d.	n.d.	n.d.
NiO	value	0.39	0.44	0.39	0.37	0.36	0.40	0.46	0.40	0.41	0.34	0.41	0.42
Total		101.2	99.0	100.0	98.8	99.3	99.6	99.6	98.8	99.6	99.3	99.4	99.6
Mg#	value	90.1	90.3	90.3	91.0	90.9	91.6	91.3	90.7	91.4	91.3	91.0	90.9
Cr#	value	90.1	90.3	90.3	91.0	90.9	91.6	91.3	90.7	91.4	91.3	91.0	90.9

Table 6. Mean orthopyroxne compositions of mantle peridotite measured by EDS [wt.%]

		Group 1						Group 2					
Sample		DKR1165	DKR1166	DKR1289	BDH-06	BDH-03(71)	BDC-15/01	BDH-13(m)	BDH-12	BDH05_2(F)	BDH-05(e)	BDC-5/10	BDH-18
n		3	5	3	3	4	2	3	4	3	3	3	3
SiO_2	value	54.3	54.6	54.0	54.0	53.8	55.2	54.3	54.4	54.6	55.1	55.2	55.1
TiO_2	value	0.08	0.14	0.14	0.10	0.11	0.10	0.10	0.06	0.07	0.06	0.05	0.03
Al_2O_3	value	4.23	3.92	3.80	3.96	4.16	3.13	3.67	3.13	3.34	2.88	2.10	1.18
Cr_2O_3	value	0.52	0.48	0.56	0.53	0.67	0.56	0.78	0.80	0.79	0.74	0.71	0.72
FeO_{tot}	value	6.57	6.41	6.34	6.39	6.30	6.35	5.82	5.98	5.59	5.60	5.70	2.07
MnO	value	0.17	0.16	0.16	0.16	0.15	0.19	0.13	0.16	0.13	0.14	0.16	0.15
MgO	value	32.8	33.2	32.7	32.7	32.2	34.0	32.9	32.9	33.3	33.8	33.3	18.2
CaO	value	0.88	0.70	0.89	0.90	1.58	0.64	1.27	1.50	1.42	0.83	1.68	24.27
NiO	value	n.d.	n.d.	n.d.	n.d.	n.d.	n.d.	n.d.	n.d.	n.d.	n.d.	n.d.	n.d.
Total		99.5	99.5	98.5	98.7	98.9	99.9	99.0	99.0	99.2	99.0	99.2	101.5
Mg#	value	89.9	90.2	90.2	90.1	90.1	90.5	91.0	90.8	91.4	91.5	91.2	94.0
Cr#	value	7.5	7.7	8.9	8.2	9.9	10.7	12.5	14.6	13.7	14.6	18.5	28.6

Table 7. Mean clinopyroxene compositions of mantle peridotite measured by EDS [wt.%]

Sample		Group a hazrburgites						Group a hazrburgites					
		DKR1165	DKR1166	DKR1289	BDH-06	BDH-03(71)	BDC-15/01	BDH-13(m)	BDH-12	BDH05_2(F)	BDH-05(e)	BDC-5/10	BDH-18
n		3	5	3	3	4	3	4	3	3	3	3	1
SiO_2	value	51.3	51.0	51.2	50.7	50.8	51.6	51.9	51.7	52.0	51.9	52.1	55.1
TiO_2	value	0.34	0.30	0.35	0.25	0.18	0.21	0.15	0.13	0.19	0.20	0.08	n.d.
Al_2O_3	value	5.66	5.10	5.10	4.62	4.99	3.60	3.62	3.93	3.55	3.28	2.75	1.18
Cr_2O_3	value	0.89	0.84	0.83	0.90	1.00	0.90	1.15	1.23	1.20	1.22	1.35	0.72
FeO_{tot}	value	2.85	2.60	2.73	2.67	2.78	2.26	2.25	2.60	2.22	2.18	2.59	2.07
MnO	value	n.d.	n.d.	n.d.	n.d.	n.d.	n.d.	n.d.	n.d.	n.d.	n.d.	n.d.	n.d.
MgO	value	16.1	16.2	16.1	16.4	17.1	16.8	16.8	17.3	16.9	16.6	18.8	18.2
CaO	value	22.1	22.1	22.3	22.6	21.9	23.5	23.0	22.3	22.7	22.9	21.0	24.3
NiO	value	0.61	0.62	0.66	0.31	0.26	0.18	0.37	0.23	0.44	0.49	0.41	n.d.
Total		99.9	98.7	99.2	98.5	99.0	99.1	99.2	99.5	99.3	98.8	99.2	101.5
Mg#	value	91.0	91.8	91.3	91.6	91.7	93.0	93.0	92.3	93.1	93.1	92.8	94.0
Cr#	value	9.6	9.8	9.7	11.6	11.9	14.5	17.5	17.4	18.2	19.8	24.8	28.6

Table 8. Major element compositions of amphibole from Group 2 samples [wt.%]

Point	Phase	SiO_2	TiO_2	Al_2O_3	Cr_2O_3	FeO_{tot}	MnO	MgO	CaO	Na_2O	K_2O	Total
#1	Paragasite	44.59	0.554	13.42	2.19	2.72	0.025	18.1	12.61	2.12	0.01	96.339
#2	Edenite	46.43	0.508	11.9	0.992	3.09	0.039	19.23	12.64	2	0.003	96.832
#3	Paragasite	44.18	0.86	14.07	2.09	3.11	0.032	18.18	12.66	2.4	0.007	97.8

Point	Atoms per formular unit (O=23)														
	Si	Al^{IV}	Ti	Al^{VI}	Cr	Fe^{3+}*	Fe^{2+}	Mn	Mg	Ca	Na	K	Sum	Mg/(Mg+Fe)	Na+K
#1	6.3	1.7	0.1	0.6	0.2	0.2	0.0	0.0	3.8	1.9	0.6	0.0	15.6	0.99	0.64
#2	6.5	1.5	0.1	0.5	0.1	0.3	0.0	0.0	4.0	1.9	0.6	0.0	15.5	1.00	0.59
#3	6.2	1.8	0.1	0.5	0.2	0.3	0.0	0.0	3.8	1.9	0.7	0.0	15.6	0.99	0.66

Table 9. $D^{mineral/silicate}$ melt for highly siderophile elements

phase	olivine	orthopyroxene	clinopyroxene	spinel	sulfide (Max)	sulfide (Min)
Os	0.03 [1]	-	0.08 [6]	-	1150000 [9]	30000 [11]
Ir	2 [2]	0.6 [5]	-	1 [8]	1900000 [9]	26000 [11]
Ru	2 [3]	-	-	4 [8]	485000 [9]	6400 [11]
Pt	0.01 [2]	-	0.1 [7]	0.2 [8]	3450000 [9]	2000 [12]
Pd	0.006 [3]	0.0051 [5]	-	0.2 [8]	536000 [9]	200 [12]
Re	0.01 [4]	0.1 [4]	0.3 [4]	0.1 [4]	800 [10]	50 [13]

References for partition coefficients data are as follows: 1 = Burton et al. (2002); 2 = Brenan et al. (2005); 3 = Brenan et al. (2003) ; 4 = Mallmann and O'Neill (2007); 5 = Zhang and Li (2022); 6 = Watson et al. (1987); 7 = Brean et al. (2016); 8 = Brenan et al. (2012); 9 = Mungall and Brenan (2014); 10 = Brenan (2008); 11 = Fleet et al. (1996); 12 = Luguet and Reisberg (2016); 13 = Fonseca et al. (2007)

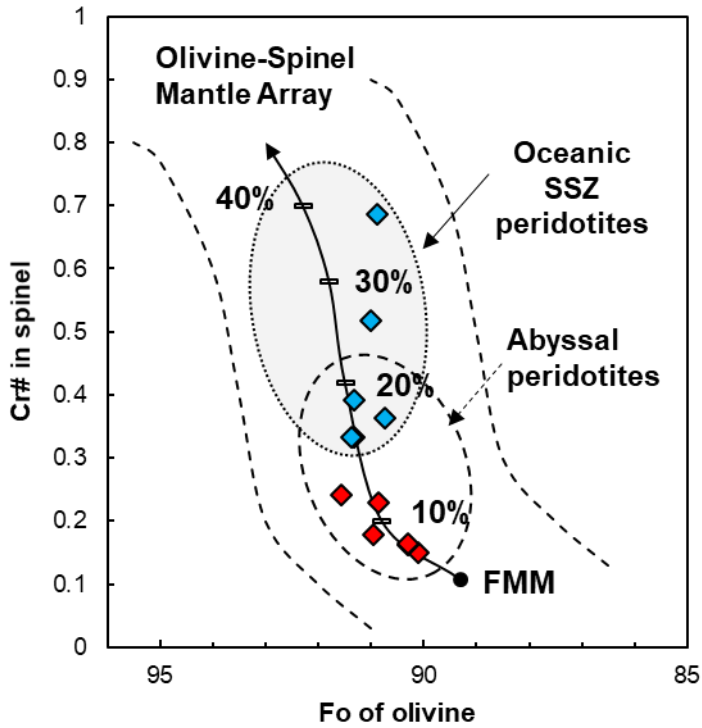

Figure 14. Olivine-spinel mantle array from Arai (1991) plotted alongside with Kalaymyo peridotites. Dashed white and dotted grey areas represent the field of abyssal peridotites (Dick and Bullen, 1984) and SSZ peridotites (Pearce et al., 2000), respectively. FMM denotes fertile MORB mantle. The degree of partial melting is shown by a solid line after Jaques and Green (1980).

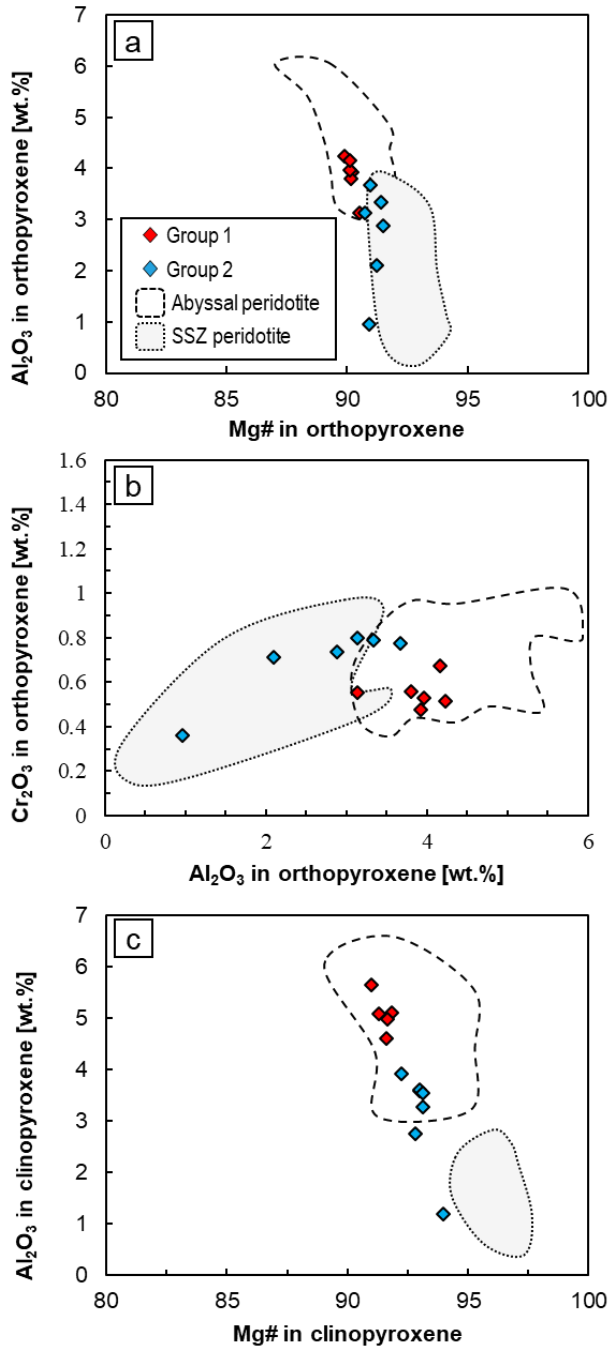

Figure 15. Mineral compositions of Kalaymyo peridotites. (a) Mg# vs. Al_2O_3 of orthopyroxenes. (b) Al_2O_3 vs. Cr_2O_3 of orthopyroxenes. (c) Mg# vs. Al_2O_3 clinopyroxenes. Orthopyroxene and clinopyroxene compositional fields for abyssal peridotites and forearc peridotites are from Dupuis et al. 2005, and references therein.

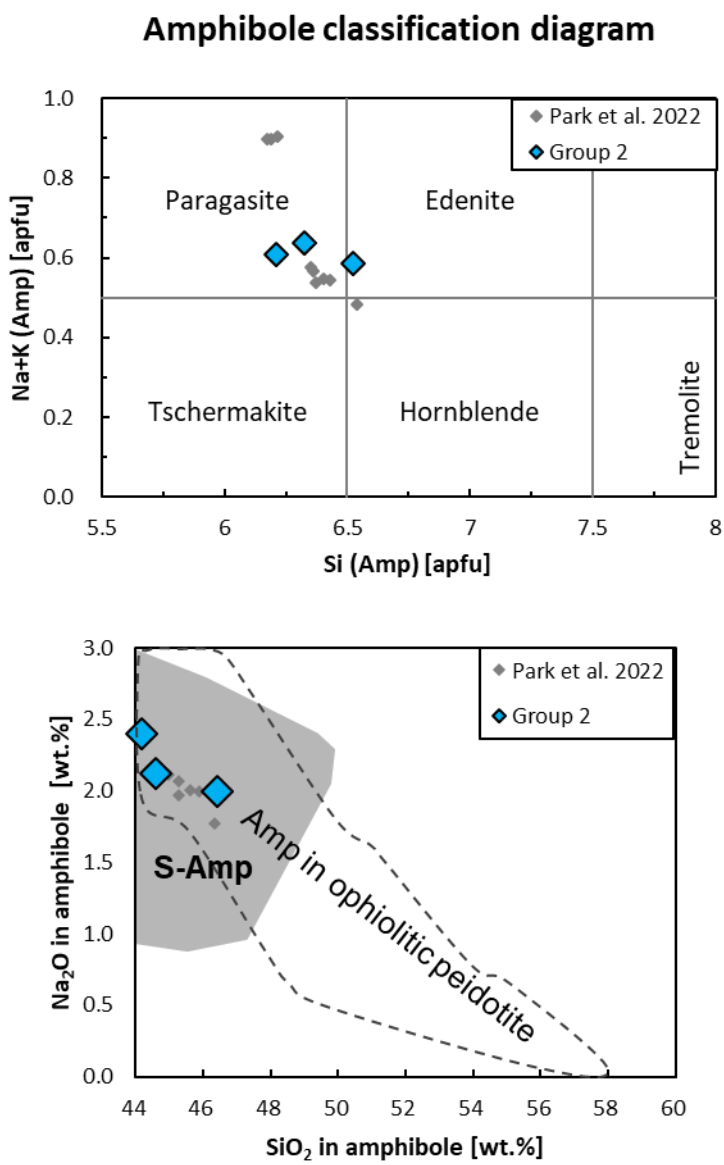

Figure 16. Diagrams for (a) classification and (b) compositional variations of amphibole in Kalaymyo peridotites. The amphibole classification diagram is after Leake et al. (1997). The fields of suprasubduction amphibole (S-amp) and ophiolitic peridotite are from Coltorti et al. (2007) and Pan et al. (2022), respectively.

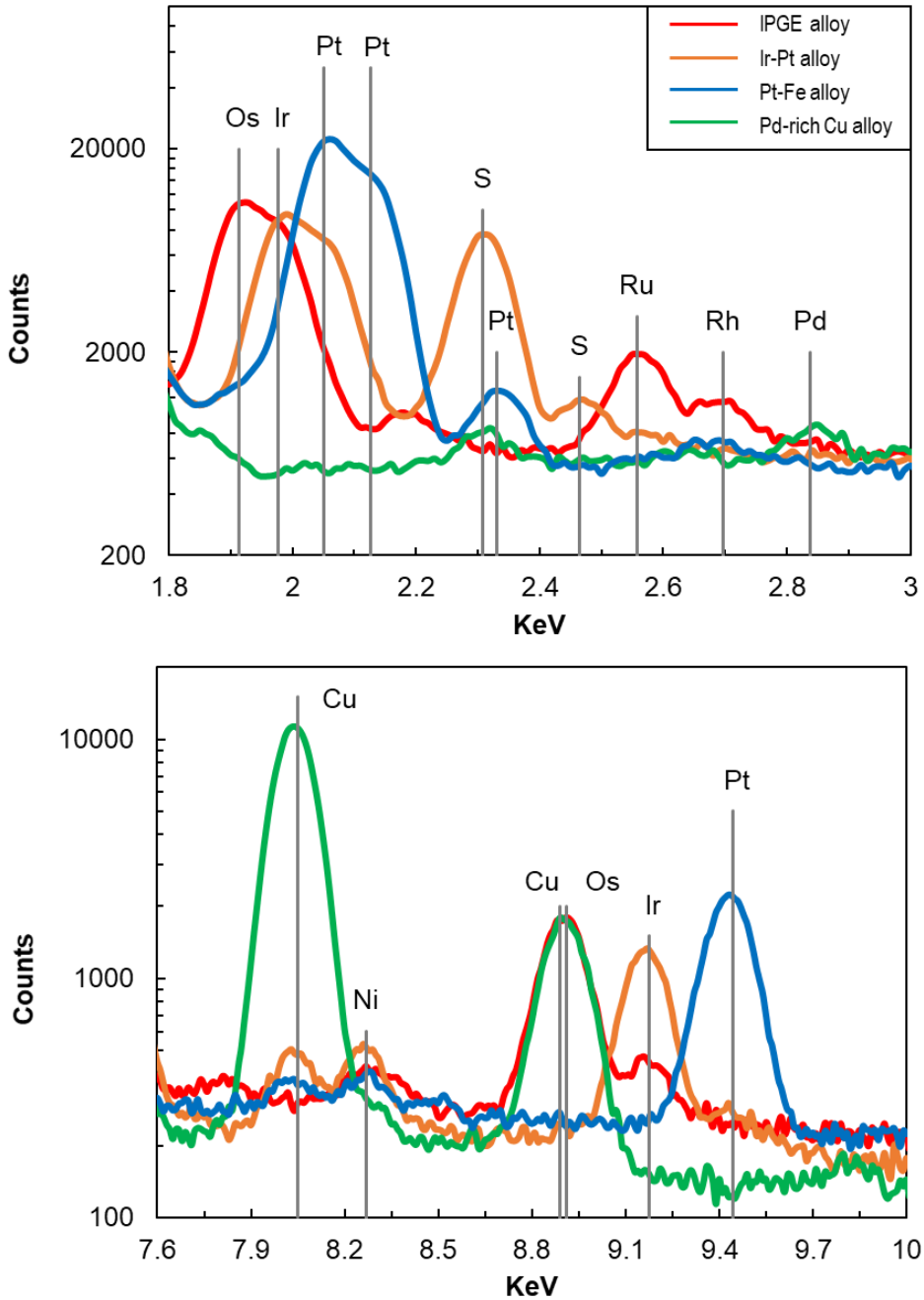

Figure 17. The energy dispersive spectra (EDS) of (a) the M shell X-ray lines of Os, Ir, and Pt, the K shell line of S, and the L shell lines of Rh, Ru, and Pd and (b) the K shell line of Cu and Ni and the L shell lines of Os, Ir, and Pt.

Chapter 5. Discussion

5.1. Effects of seawater weathering and serpentinization

Ophiolitic peridotites may undergo varying degrees of seawater weathering (0-100℃) and serpentinization (25-400℃). Such alterations can affect mineral assemblages and geochemistry of the rocks (Snow & Dick, 1995; Bach et al., 2004; Paulick et al., 2006; Klein et al., 2013; Malvoisin 2015). Seawater weathering in an oxidizing environment leads to the formation of alteration minerals, including iddingsite and carbonate veins (Bach et al., 2004), and results in the destabilization of sulfide, which is the dominant host of HSEs in peridotites, transforming it into metal oxides (Becker and Dale, 2016). As no oxidative veins were observed and the weathered surfaces of rock specimens were excluded in this study, the influence of seawater weathering on whole-rock HSE geochemistry can be excluded in this study.

However, the samples used in this study have undergone varying degrees of serpentinization. The majority of samples exhibit minimal alteration based on petrographic observations. They contain only small amounts of alteration minerals, and their grains have an intact portion of over 50% on average. However, DKR1289 and BDC-5/10 display significant serpentinization, with an intact portion of less than 50%. The degree of serpentinization can also be estimated by LOI (loss of ignition). Most of the peridotite samples have a small LOI of < 5%, suggesting the limited degree of serpentinization. However, samples DKR1289 and BDC-5/10 have high LOI values of 7.1 and 10.2% respectively, indicating that they are more serpentinized. The Kalaymyo peridotites predominantly plot below the ‘terrestrial array’ (Zindler

and Hart, 1986) in the Al_2O_3/SiO_2-MgO/SiO_2 diagram (Fig. 8B), representing a Mg loss during the process of serpentinization (Niu, 2004)

Serpentinization also affects the stability of host minerals of HSEs. The studied samples contain alloys such as awaruite and native coppers, along with characteristic serpentinization minerals like serpentine and magnetite (Fig. 4, 5). Serpentinization processes result in desulfidation, transforming minerals from Fe-Ni sulfide and Cu-rich sulfide into awaruite and Cu-rich alloys, respectively (Fig. 5) (Klein and Bach 2009; Schwarzenbach et al., 2021; Eslami et al., 2021).

Previous studies have suggested that serpentinization may interrupt the $^{187}Os/^{188}Os$ ratio (e.g., Snow & Reisberg, 1995; Standish *et al.*, 2002) and concentration of Re and Pd (e.g., Luguet *et al.*, 2003; Harvey *et al.*, 2006). For example, seawater has a higher Os isotope ratio (~1.06; Levasseur et al., 1998) than peridotites (e.g., 0.1296 ± 6, Primitive Upper Mantle; Meisel et al. 2001), but low Os concentrations of seawater (3.8 fg/g; Sharma et al. 1997) is not enough to disrupt Os isotope ratio of peridotite. The effect on Re and Pd was accounted for by their mobility in fluids (e.g., Luguet et al., 2003, Harvey et al., 2006). However, recent studies have suggested that these are not affected by serpentinization but may be influenced by sampling bias, as there is no correlation with LOI even in highly serpentinized rocks (e.g., Liu *et al.*, 2008; Day *et al.*, 2017).

The results from Kalaymyo peridotites suggest that there is no significant correlation between LOI, HSE and Os isotope (Fig. 14, 15). This lack of correlation may indicate that the transformation from sulfide to alloy through desulfurization does not significantly influence the HSE and Os isotope composition at whole-rock scale, because they remain stable under reducing conditions during serpentinization (Snow & Schmidt, 1998; Becker et al., 2006; Liu et al., 2009; Marchesi et al., 2013).

A slight negative correlation between Pd and LOI could potentially a result of sampling bias. Furthermore, negative correlation between Re and LOI of serpentinized peridotites indicates that serpentinization does not increase Re contents as confirmed by previous study (e.g., Becker et al., 2006; Liu *et al.*, 2008; Day *et al.*, 2017) Therefore, the whole-rock HSE and Os isotopes observed in this study can be considered as the primary magmatic signature, independent from the secondary alteration processes.

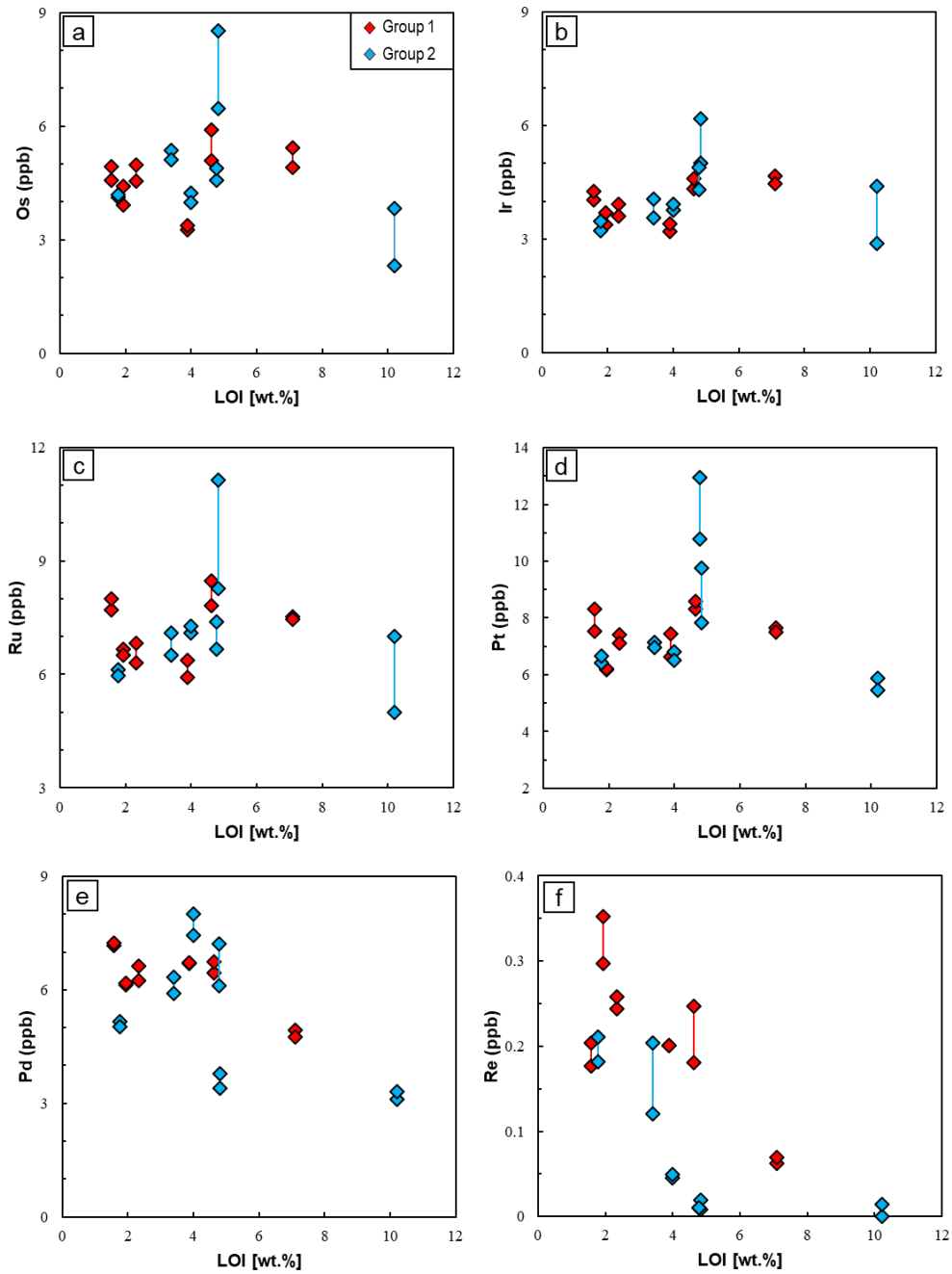

Figure 18. Covariation of the concentrations (in ppb) of HSEs against LOI (wt.%) for Kalaymyo peridotites.

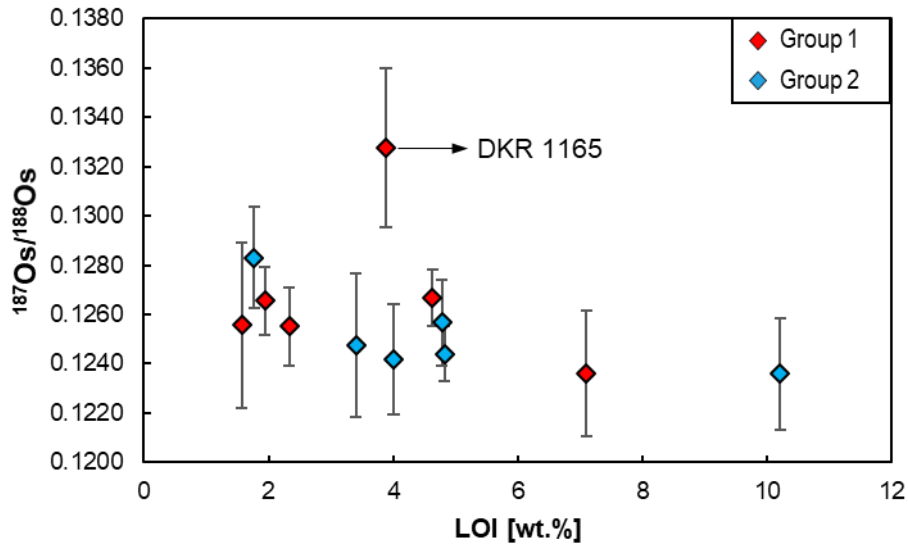

Figure 19. Covariation of the Os isotopic ratio against LOI (wt.%) for Kalaymyo peridotites.

5.2. Partial melting of Kalaymyo peridotites

Partial melting is a crucial magmatic process that occurs in the mantle and plays a significant role in governing the concentration of HSEs. Therefore, it is essential to quantify the degree of partial melting before discussing the concentration of peridotites during partial melting. Park et al. (2022) calculated the degree of melting based on the Cr# of spinel. However, this approach indirectly represents the degree of melting and Cr# of spinel in Group 2 samples can be significantly affected by the mantle-melt interaction. Thus, it is necessary to select another index that can directly and accurately represent the degree of partial melting before discussing the mantle HSE content.

In this study, I inferred the degree of partial melting by using whole-rock Al_2O_3 content, a commonly used indicator of partial melting in mantle rocks, based on the bulk partition coefficient suggested by Niu (1997). As a result, Group 1 samples are estimated to have undergone ~3.1–15.0% partial melting, while Group 2 samples have undergone 15.1–20.9% partial melting from the preferred mantle source (Niu 1997). Although the whole-rock Al_2O_3 content can be lowered by the mantle-melt interaction after partial melting, the degree of partial melting obtained through this method shows a good correlation with the results inferred from the whole-rock HREE melting model (Fig. 20). Hence, the whole-rock Al_2O_3 content can be used as an indicator of the minimum degree of partial melting.

Partial melting has an overall effect on the whole-rock and mineral composition, making it useful for tracking the partial melting history (e.g. Dick and Fisher, 1984). Since melting occurs from minerals with a low melting point, clinopyroxene is

exhausted first, at least in the melting of spinel lherzolitic peridotites, followed by the melting of orthopyroxene and olivine. The whole-rock chemical composition reflects the predominant melting of clinopyroxene. As clinopyroxene and orthopyroxene melt predominantly, the whole-rock SiO_2, TiO_2, CaO, and Al_2O_3 contents are reduced with melting, and MgO, which is abundant in the remaining olivine, tends to increase. As seen in Fig. 7, this trend means that the partial melting degree gradually increases as it changes from Group 1 to Group 2. In the mineral chemical composition, Fo and Mg# gradually increases while Al_2O_3 gradually decreases (Fig. 14 and 15). Additionally, in the spinel composition of Group 1, Cr# and TiO_2 show a negative correlation (Fig. 3). This indicates that, as mentioned in Park et al. (2022), the chemical composition of Group 1 samples was differentiated based on the partition coefficient of each element during partial melting, and there was limited effect of the mantle-melt interaction in Group 1 samples.

Platinum group elements are classified into two groups according to the melting point and similar geochemical behavior; IPGEs with a melting point higher than 2000℃ and PPGEs with a melting point lower than 2000℃ (Barnes et al., 1985, Woodland et al., 2002). The PGEs are mainly included in sulfides due to their strong chalcophile affinity and are greatly influenced by the sulfide phase during various geological processes in the oceanic mantle (Barnes et al., 1997).

There were two scenarios for understanding the behavior of HSEs during the partial melting of mantle rocks. The first scenario suggests that sulfide matte is produced by high-temperature and high-pressure melting, where HSEs are controlled by their $D^{sulf/sil}$ and dominated by sulfides (Fonseca et al., 2011; Mungall and Brenan, 2014). If these partition coefficients are different among HSEs, they might cause fractionation during mantle melting. The second scenario involves partial melting of

the upper mantle at relatively low temperatures, resulting in the preferential removal of Cu-rich sulfide melt by incongruent melting of sulfide (Bockrath et al., 2004). During partial melting of sulfide, IPGE is predominantly distributed in Fe-enriched MSS (monosulfide solid solution; $[Fe, Ni]_{1-x}S$), while PPGE is distributed in Cu-enriched ISS (intermediate solid solution; $[Cu, Fe]_{1-x}S$) (Bockrath et al., 2004; Brenan et al., 2016). This selective separation leads to a decrease of PPGE over IPGE in the residual mantle, resulting in the enrichment of IPGE relative to PPGE and a gradual decrease in the Pd/Ir ratio during the partial melting of the mantle. However, recent experiments on a range of sulfide contents indicate that sulfide exists as a partially to totally molten state at upper mantle conditions (Zhang and Hirschmann, 2016). Therefore, the first scenario should be adopted for tracing the HSE composition of ophiolitic peridotites.

The change in HSE according to partial melting can be investigated by plotting the whole-rock Al_2O_3 content in a binary diagram together with the analyzed HSE concentration. The partial melting model utilized in this study is based on a near-fractional melting model, as described by Rehkämper et al. (1999). The model follows a specific procedure consisting of several steps. First, a small melt fraction of 1% is generated through non-modal batch melting. Next, this melt fraction is completely separated from the residual material. Finally, an additional increment of 0.1% melt fraction is introduced to the depleted mantle source. The initial modal abundances and melting reaction coefficients used in the model are consistent with those presented in the work of Rehkämper et al. (1999). The HSE composition of the melting model starts from the primitive upper mantle of Becker et al. (2006). Sulfur content of the initial mantle is assumed to be 150 ppm (O'Neill, 1991) and the sulfur concentration of the melt removed is set to 1000 ppm (Mavrogenes and O'Neill,

1999). Thus, sulfur and sulfide are completely exhausted at 18% melting in this model. The degree of partial melting (%) is also converted to Al_2O_3 using Niu (1997). The partition coefficient between silicate mineral and silicate melt is also considered in this model as green lines. Detailed assumptions such as partition coefficients between sulfide and silicate melts are presented in Fig. 11 along with the results of PGE and Re partial melting models. In the model, as the degree of partial melting increases, elements with high partition coefficients for the sulfide melt increase (Fig. 11a, b, c), and elements with low values tend to decrease (Fig. 11d, e, f). The sulfide model rapidly decreases around the Al_2O_3 content of ~1 wt.% because the sulfide in the mantle is exhausted and PGEs no longer remain and escape from the rock.

Based on the analyzed data, the IPGEs such as Os, Ir, and Ru behave in a manner that is consistent with their high partition coefficient. The data shows that their content in the residual mantle generally increases with an increasing degree of partial melting. The partition coefficients between sulfide liquid and silicate melt ($D^{sulf/sil}$) used in the melting model range from thousands to millions, which is in agreement with previous studies (Fleet et al., 1996; Mungall and Brenan 2014).

The PPGE content in Group 1 shows a consistent or slightly decreasing trend. This is best explained by a $D^{sulf/sil}$ value of 3000, which corresponds to the low partition coefficients in the range of 2000 to 6000 as proposed by Zhang and Li (2021). This is also supported by data from abyssal peridotites compiled by Barnes et al. (2015) (Fig. 11d, e). One possible explanation for this discrepancy is that the melting started from a lower concentration. However, it is difficult to explain this decreasing trend solely by lower starting composition with the single phase melting model. Instead, it may be plotted between the models with the high (Mungall and Brenan, 2014) and low distribution coefficient (200; Luguet and Reisberg 2016).

Therefore, it is possible that the concentration of Pt and Pd is controlled by other partition coefficients.

On the other hand, the PPGE content in Group 2 exhibits higher values than predicted by the melting model. While it could be explained by high partition coefficients similar to IPGE, it is more likely that the higher PPGE content in Group 2 is a result of mineral precipitation due to mantle-melt interaction, which seems to be a more plausible process.

The partition coefficient of Re is varied with fO_2 and fS_2 conditions, with reported values ranging from 1 to 50 by Fonseca et al. (2012) and 400 to 800 by Brenan (2008). Thus, rhenium is characterized to be less partitioned to sulfide compared to PGEs. Therefore, the whole-rock Re content is expected to decrease significantly as partial melting proceeds. As shown in Fig. 11f, the whole-rock Re content tends to decrease to a lower value than the melting model and does not increase in Group 2, indicating that Re was depleted by partial melting and was not significantly introduced in the subsequent magma activity.

The whole-rock HSE melting models that consider the partition coefficient between silicate mineral and silicate melt (silicate melting model) are also suggested as green lines with the sulfide melting model (Fig. 11). The silicate melting model does not significantly differ from the sulfide melting model before sulfides are exhausted. However, the high compatibility of IPGE for olivine can explain the residual high IPGE concentration of Group 2 samples. On the other hand, the low compatibility of PPGE for olivine does not strongly affect the sulfide melting model, which means that PPGE cannot remain in residue after sulfide exhaustion occurred.

It is known that PGEs present in sulfides are redistributed to other phases by the decomposition of sulfide during desulfurization by partial melting (Luguet et al.,

2007; Lorand et al., 2010; O'Driscoll and González-Jiménez 2016). According to the melting model, Group 2 samples with Al_2O_3 less than ~1 wt.% are expected to have any primary sulfide remained, as it is exhausted at Al_2O_3 content ~1 wt.%. During the process of partial melting of sulfides, Pt and Pd are preferentially removed from sulfides due to their relatively lower partition coefficient to sulfides. Furthermore, Pt remains as a Fe-Pt-Ir alloy, while Pd is removed in the form of a Cu-Ni sulfide melt, which has been experimentally confirmed by Peregoedova et al. (2004). This can be observed in the Kalaymyo sample through the decrease in Pd/Pt throughout the sample due to partial melting (Fig. 17b). Additionally, in the correlation chart between PGEs, Ir shows a correlation with all but Pd, which supports the distribution of Os-Pt to related mineral assemblages and Pd to other phases (Fig. 13). Therefore, it is likely that the content of PGEs other than Pd in Group 2 is controlled by platinum group minerals (PGMs).

The IPGE-bearing minerals in the residual mantle are known as Pt-Ir alloy, Os-Ir-Ru alloy, and Ru-Os-bearing sulfide (O'Driscoll and González-Jiménez, 2016, and references therein). These phases are expected to be stable at the degree of partial melting just before the liquid sulfide in harzburgites is consumed in the process of experimentally lowering fS_2 (e.g., Fonseca et al., 2012; Mungall and Brenan, 2014; Brenan et al., 2016). The IPGE-containing minerals, such as Fe-Os-Ir-Ru alloy and Ir-Pt sub-grain (Fig. 6e, Fig. 17), found in Group 2 support that this kind of PGE distribution occurred in these samples, resulting in a high IPGE content heterogeneity between Group 2 duplicate analyses due to the nugget effect of PGM.

To reduce the nugget effect of sulfide, the ratio of PGE can be used since the absolute concentration of PGE may be affected by this phenomenon (Rehkämper et al., 1999). In Group 1 samples, the Pd/Ir ratio and Pd content are best explained by

a melting model from the PUM with a Pd $D^{sulf/sil}$ of 3000 (Fig. 11e, 21a), which is consistent with the range of 2000-6000 suggested by recent experiments (Zhang and Li, 2021) and is considered suitable for low PGE content in the unit of several ppb. However, some Group 2 samples (BDH-05_2(F), BDH-18) show high Pd/Ir ratios that do not match the model (Fig. 11e, 21a), indicating that the Pd/Ir ratio in Group 2 was controlled not only by partial melting but also by additional magma activity.

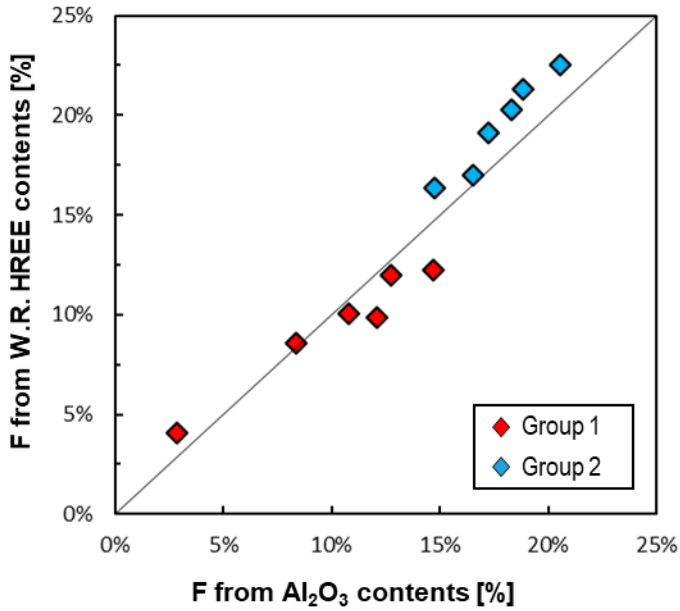

Figure 20. Covariation of the degree of partial melting (%) from Niu et al. (1997) and Johnson et al. (1990) for Kalaymyo peridotites**.**

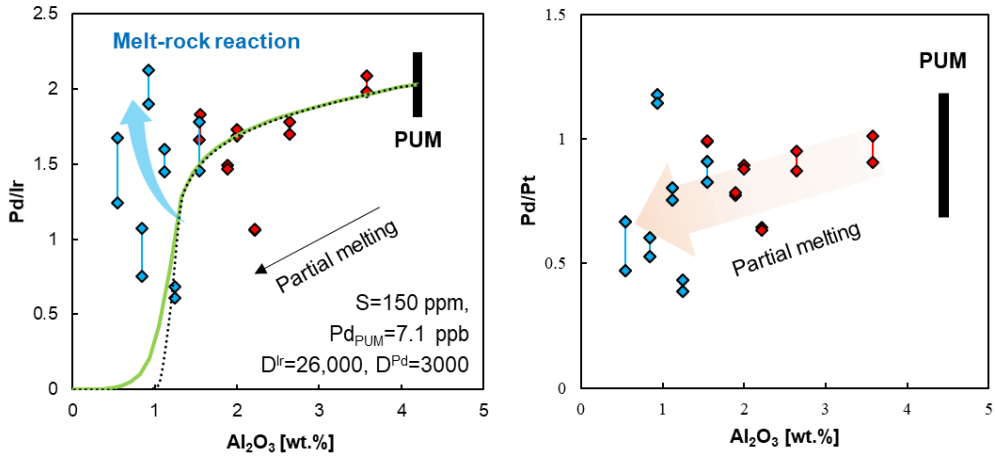

Figure 21. Variations of (a) Pd/Ir and (b) Pd/Pt with respect to whole-rock Al_2O_3 contents in peridotites. The symbols and melting models applied here correspond to those used in Fig. 11

5.3. Mantle-melt interaction

The preceding discussion indicates that Group 2 samples underwent post-melting reactions. Ophiolitic peridotites are subject to various mantle-melt interaction that alter their lithology, texture, and chemical compositions during their evolution and exhumation processes (Dilek and Furnes, 2014, and references therein). Melts that react with ophiolitic peridotites can affect variously on the host peridotite. For instance, MORB is known to precipitate secondary clinopyroxene and plagioclase in the reacted mantle and significantly increase the TiO_2 contents of spinel (Saunders and Tarney, 1979). Conversely, the subduction-related boninitic melt, which forms by melting the highly depleted mantle, is rich in compatible elements such as Mg and lacks incompatible elements such and Ti, leading to the dissolution of pyroxene in the reacted rock and the precipitating olivine (Zhou and Robinson, 1997). By examining the mineral and chemical compositions of the rock, it is possible to trace the characteristics of the melt.

The previously studied Kalaymyo peridotites exhibit distinct textural and geochemical characteristics in peridotites, which can be attributed to the degree of partial melting as well as various mantle-melt interactions (Liu et al., 2016b; Park et al., 2017; Niu et al., 2018; Park et al., 2022). Niu et al. (2018) reported evidence of a mantle-melt interaction between Kalaymyo peridotites and MORB, based on the olivine inclusions in orthopyroxene. In contrast, Liu et al. (2016b) and Park et al. (2017) revealed a gradual increase in the amount of olivine towards dunite, suggesting a selective dissolution of pyroxene by the Mg-rich melt (Zhou and Robinson, 1997). Additionally, Park et al. (2017) suggested that this melt not only

transformed spinels from anhedral to euhedral shapes but also contributed to an increase in their components, such as TiO_2.

Evidence of mantle-melt interactions are also observed in the Group 2 samples. Park et al. (2022) suggested that olivine appears as embayment and ovoidal inclusions in pyroxene, and as neoblast near porphyroclastic primary silicates. Primary pyroxene is replaced by olivine and amphibole (Fig. 5c, d). These petrographic pieces of evidence indicate significant reaction of Group 2 samples with Mg-rich melts. Additionally, the presence of paragasitic amphibole suggests that this melt is a hydrous subduction zone melt (Fig. 16). Geochemical analysis from Park et al. (2022) also reveals that both whole-rock and mineral major elements fall within the range of SSZ peridotite (Fig. 7), and the trend between Cr# and TiO_2 of spinel shows a positive correlation towards boninitic-IAT (Fig. 3). These petrographic and geochemical changes demonstrate that subduction-related melts had a significant effect on Group 2 samples.

Mantle-melt interactions can also have variable effects on the whole-rock content of HSE (Luguet and Reisberg, 2016 and references therein). Since HSE are highly chalcophile, their changes are largely dependent on the S-saturation of the reacted magma. If the magma is S-saturated, it is known to precipitate additional sulfide and introduce HSE into the rock (e.g. Dai et al., 2011). On the other hand, S-undersaturated melt is known to dissolve sulfide and deplete HSE (e.g. Liu et al., 2010; Xu and Liu 2019).

Based on the previous discussion, it is evident that the Group 2 samples have undergone a mantle-melt interaction with arc-related basaltic melt, as indicated by the euhedral shape and positive correlation between TiO_2 and Cr# of spinel (Fig. 3, 4d) and amphibole replacing primary silicates (Fig 5c, d). While these reactions are

typically associated with S-undersaturated conditions (Hamlyn et al., 1985), the saturation of sulfur is influenced by various mechanisms, and there are cases where basaltic melts have precipitated sulfides in the mantle (Dai et al., 2011).

The precipitation of sulfides can significantly affect the PPGE content and Pd/Ir ratio. Some Group 2 samples have the Pd/Ir ratios higher than the expected value from partial melting models (Fig. 21a), and there are large differences in Pd contents between duplicate analyses (Fig. 11e). Unlike other PGEs, Pd has a high solubility in silicate melt and does not form an alloy (Mungall and Brenan, 2014 and references therein). Therefore, the difference in Pd content between duplicate analyses is unlikely to be caused by Pd alloy formation. Additionally, the effect of residual sulfide can be ruled out as the primary sulfide has already been exhausted by partial melting in the highly depleted Group 2 samples. These observations suggest that the Pd content of Group 2 sample was controlled by the addition of secondary sulfide.

As a result of the mantle-melt interaction between depleted residual mantle and a pyroxene-undersaturated melt accompanied by sulfide addition, the whole-rock Al_2O_3 content decreases, and Pd/Ir increases. The observed high Pd/Ir ratio can be successfully modeled by considering the introduction of sulfides derived from melts, as illustrated in Fig. 22. The calculation parameters used in the model are based on the work of Rehkämper et al. (1999), with an assumption of 50 ppm segregation of sulfide liquid for each melt ratio (X_{melt}/X_{res}). The starting point of the model is determined based on the most depleted sample in terms of Pd content. The PGE concentration of sulfide is determined using partition coefficients based on sulfide saturation (as presented in Table 4 of Rehkämper et al., 1999). The calculated Pd/Ir values of Group 2 samples align well with the sulfide from sulfide undersaturated

melts (Sulfide addition D). According to the model, the mantle-melt interaction with X_{melt}/X_{res} ratios ranging from 0 to 3 can account for the observed increase in Pd/Ir in Group 2 samples. This process successfully replicates the significant variation in Pd and Pd/Ir ratios observed in Group 2 samples as a result of the mantle-melt interaction.

On the other hand, the negative correlation between IPGE and Cu in Group 2 suggests that IPGE was not significantly introduced in the form of secondary sulfide by the mantle-melt interaction (Fig. 23b). This is because added composition does not have enough Ir abundances to enhance whole-rock Ir components. Microscale textural evidence further confirms the addition of Pd. Primary silicate minerals in Group 2 samples were observed infiltrated by amphibole (Fig. 6b, d), and interstitial Cu-Ni alloy is precipitated between the rim of amphibole and the cleavage of clinopyroxene, which has a high Pd concentration (~1000ppm). The Cu-Ni alloy is thought to undergo desulfurization by serpentinization after being precipitated from the melt.

Platinum is predominantly found in the form of alloys in the supra-subduction zone mantle with low fS_2 and high fO_2 (Defant and Kepezhinskas, 2001; Kepezhinskas et al., 2002; Xu and Liu, 2019). Platinum exists as a sulfide or alloy in the residual mantle and remains relatively constant during partial melting in Group 1 samples (Fig. 11d). In contrast, in Group 2 samples, it is increased from the melting model like Pd. The addition of Pt is supported by Pt-Fe alloy included in paragasitic amphibole (Fig. 6d). The origin of the Pt-Fe alloy in the depleted mantle is generally attributed to subsolidus decomposition of sulfide, but in Group 2, it is also observed as inclusion in metasomatic mineral (Fig. 6d). This is not surprising, as Pt is stable in the alloy region in the subduction zone environment (O'Driscoll and González-

Jiménez 2016). Therefore, this suggests that Pt was introduced in the form of an alloy by the subduction zone melt.

The IPGE alloy observed in this study provides important insights into the behavior of PGEs during the mantle-melt interaction. The alloy is predominantly composed of IPGEs and has a length of 8 μm in the major axis and 3 μm in the minor axis (Fig. 6e). This alloy is not associated with fluid-mobile elements, which rules out the possibility of it being a product of alteration. The host sulfide of the IPGE alloy is euhedral and has an assemblage of pyrrhotite and exsolved pentlandite, which is indicative of the decomposition of the original magmatic sulfide due to lowering temperatures (Becker and Dale 2016; Mansur et al. 2021). The sulfide is also rimmed with magnetite and awarutite (Fig. 6e), which is a common mineral assemblage observed during the serpentinization of base metal sulfides (Klein and Bach, 2009).

The IPGE alloy contains more than 35 wt.% of Os and shows a higher Os content than other PGEs. According to Fonseca et al (2012), Os is the least soluble element among the HSEs with a solubility of ~40 ppm in sulfide matte. Therefore, it is not uncommon for IPGE alloys to have Os-rich components when exsolved from sulfide matte. This suggests that the IPGE alloy observed in this study likely formed through the exsolution of IPGEs from sulfide matte during the high degree of partial melting. The mass balance of PGE can be confirmed by estimating the volume of this IPGE alloy. Assuming that the primary sulfide is an octahedron and the IPGE alloy is an ellipsoid, the sulfide must have an average PGE concentration of 2.5 wt.%. However, the presence of these high-PGE sulfides at the typical 0.1 modal % in SSZ peridotite is unlikely given that the typical whole-rock PGE concentration in peridotite is in the ppb range. Therefore, it is reasonable to regard the PGE

concentrated in the IPGE alloy as the result of redistribution by magmatic process rather than originating from exsolution in a single grain.

The EDS spectra of IPGE alloy exhibit a high Os peak and low Ir and Ru peak (Fig. 17), but their concentrations in the whole-rock show a good correlation (Fig. 13). This can be explained by the partitioning of Ir and Ru into residual Ir-Pt alloy and euhedral Cr spinels, respectively, as suggested by Peregoedova et al. (2004) and Park et al. (2012). The PGE hosted in PGM may be redistributed during the partial melting and mantle-melt interaction and remained constant in terms of the whole-rock concentration. In summary, it is thought that the influx of IPGE did not occur through the mantle-melt interaction, but rather the redistribution of the mineral phase containing IPGE occurred. Therefore, the concentration of IPGE is greatly influenced by the PGM alloy.

In general, when a sulfur-saturated melt reacts with the mantle to precipitate sulfide, chalcophile Re is partitioned into the sulfide, increasing the Re content of the mantle, whereas when a sulfur-undersaturated melt reacts, the primary sulfide in the mantle is dissolved, and the Re content is decreased (Luguet and Reisberg 2016). However, in the case of Group 2 samples, the Re concentration tends to decrease during mantle-melt interaction, even though secondary sulfide is introduced (Fig. 11f). While Pd is introduced by secondary sulfides, Re behaves incompatibly, despite its abundance in the melt. This suggests that other factors may affect the partitioning of Re into sulfides.

Rhenium is the least partitioned to sulfides among HSEs and behaves like a lithophile element, especially in high fO_2 environments (Mallmann and O'Neill 2007; Fonseca et al. 2007). Experimental studies have shown that in high fO_2 systems, Re is preferentially partitioned into silicate minerals rather than sulfides (Burton et al.

1999). Since Group 2 samples have reacted with a subduction-related melt that is highly oxidized (Wang et al. 2020), Re is not distributed to sulfides during the mantle-melt interaction process and behaves incompatibly. Therefore, Group 2 samples that have undergone mantle-melt interaction do not show enriched Re compositions, despite the introduction of secondary sulfides and abundance of Re in the melt.

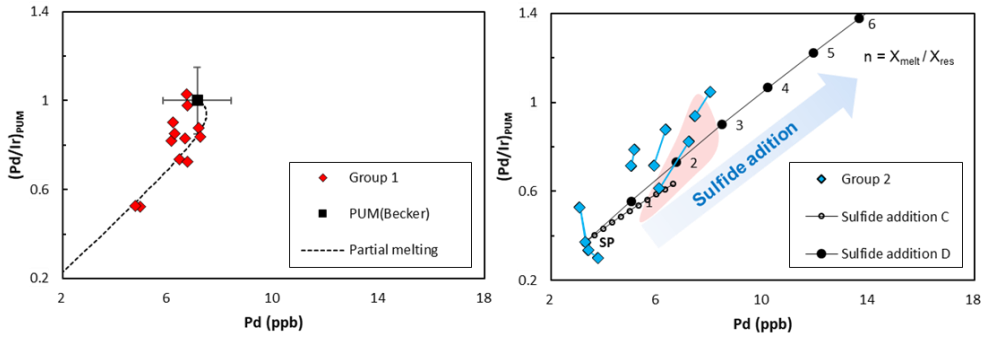

Figure 22. Variations in $(Pd/Ir)_{PUM}$ against Pd (ppb) in peridotites, examined through (a) a melting model and (b) a sulfide addition model. The numerical values on the sulfide addition line denote X_{melt}/X_{res}, symbolizing the extent of the melt-rock reaction. Red area is a compositional range of Group 1 samples. A notable alignment is observed between the Group 2 samples and the sulfide addition model D (sulfide undersaturated; Rehkämper et al., 1999).

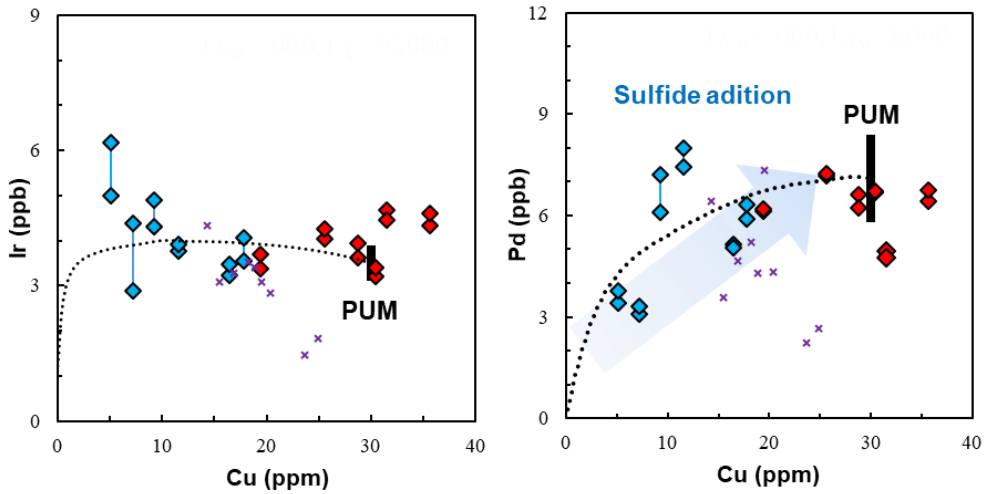

Figure 23. Variations of (a) Ir and (b) Pd contents against whole-rock Cu contents in peridotites. The $D^{sul/sil}$s of each element are 1000 for Cu, 26000 for Ir, and 3000 for Pd. The symbols and melting models employed in this figure are consistent with those in Fig. 11.

5.4. Os isotope geochemistry

The whole-rock Os isotope system is a useful tool for interpreting partial melting and mantle-melt interactions in peridotites (Reisberg 2021). In this system, the parent element Re is more incompatible than the daughter element Os, unlike in other lithophile isotopic systems such as Rb-Sr, Sm-Nd, and U-Th-Pb. As a result, the ancient Re/Os concentration and the radiogenic ^{187}Os produced in peridotites decrease with increasing degrees of partial melting. Consequently, the whole-rock $^{187}Os/^{188}Os$ ratio of peridotites also decreases with increasing degrees of partial melting (Shirey and Walker, 1998; Meisel et al., 2001).

During the mantle-melt interaction process that follows partial melting, the percolating melt with a higher Os isotopic ratio is less likely to disturb the Os isotopic composition of the host rock due to its relatively low Os concentration (0.100 ppb) compared to normal peridotites (3-4 ppb) (Walker et al., 1989; Chesley et al., 2004; Harvey et al., 2006). Therefore, a higher Os isotopic ratio is only observed when radiogenic Os is predominantly introduced by the mantle-melt interaction (Rudnick and Walker, 2009; Lorand et al., 2013). This high Os isotopic ratio serves as evidence for the introduction of radiogenic Os through melt percolation.

The Kalaymyo peridotites studied here show a range of Os isotopic ratios from 0.1239 to 0.1331, indicating some degree of heterogeneity. However, overall, the samples have lower Os isotopic ratios than the PUM value of 0.1296 (Meisel et al., 1996), indicating that there has been no significant addition of radiogenic Os. Additionally, there is no clear correlation between the Os isotopic ratios and the Al_2O_3 contents or $^{187}Re/^{188}Os$ of the whole-rock samples, as shown in Fig. 13. This

suggests that the Os isotopic variations in the Kalaymyo peridotites are not related to partial melting processes, but rather to other factors such as source heterogeneity.

Several possible explanations exist for the lack of correlation between $^{187}Os/^{188}Os$ and $^{187}Re/^{188}Os$ and whole-rock Al_2O_3 contents. First, the disturbance by the mantle-melt interaction was not occurred by a low Os concentration of melt as is commonly known. This can be supported by the global distribution of the Os isotope of the mantle wedge that radiogenic $^{187}Os/^{188}Os$ is observed with Os content less than 1 ppb (Liu et al., 2012). Alternatively, a short time (~125Ma) after melting may not have resulted in sufficient radiogenic ingrowth despite the Re/Os fractionated by partial melting. Therefore, the scattered Os isotopic ratios could be attributed to the heterogeneous nature of the mantle. The absence of correlation with other indicators suggests that they are not genetically related, but rather are located in close proximity tectonically. This is consistent with previous studies showing that the Neo-Tethyan mantle is highly heterogeneous in terms of Os isotopes (e.g., Niu et al., 2015, Xu et al. 2020). Therefore, this study provides further evidence to support the notion that the upper mantle is heterogeneous in Os isotopes (Snow and Dick, 1995; Parkinson et al., 1998; Walker et al., 2005; Harvey et al., 2006; Liu et al., 2008; Schulte et al., 2009).

Chapter 6. Summary

The Kalaymyo ophiolitic peridotites exhibit various textures and chemical compositions due to partial melting and mantle-melt interaction. For my study, I divided the samples into two groups, Group 1 and Group 2, based on their spinel compositions with a cutoff value of 0.3 Cr#. Group 1 represents peridotites that have undergone partial melting without mantle-melt interaction, while Group 2 comprises peridotites that have experienced both partial melting and mantle-melt interaction. The alteration process has some impact on major elements, but it does not affect the HSE and Os isotopic compositions.

The effects of partial melting are clearly observed in the behavior of most HSEs. In Group 1, the changes in IPGE content align well with a partial melting model, with high $D^{sulf/sil}$. On the other hand, the behavior of Pt and Pd in Group 1 is best explained by a melting model with a partition coefficient of 3000 between sulfide melt and silicate melt. The melting model including the partition coefficient between silicate minerals and silicate melt provides a better explanation for the high IPGE contents, indicating that silicate minerals can act as hosts for IPGEs after sulfide exhaustion. The significant differences in duplicate analyses of IPGE content are attributed to the existence of PGMs formed during extensive partial melting, which is supported by the presence of IPGE and Ir-Pt alloys attached to magmatic sulfide. The Re content decreases with increasing degrees of partial melting in both groups, confirming the effect of partial melting.

The effect of mantle-melt interaction is different for HSEs. The wide variation of Pd and Pt contents in Group 2 samples can be attributed to mantle-melt interaction,

which is supported by the presence of secondary sulfides and Pt-Fe alloys associated with hydrous minerals derived from subduction zones. However, the IPGE content does not show significant changes in response to mantle-melt interaction. Additionally, the reacted melt fails to introduce Re due to its high oxidation state.

The Os isotopic ratios do not show a specific correlation with the indices of partial melting or mantle-melt interaction. Most samples display sub-chondritic Os isotopic compositions, which are indicative of residual peridotites. The lack of correlation suggests the absence of ancient Re influx during the mantle-melt interaction process and the preservation of the initial isotopic composition due to the high Os content in the residual mantle. This indicates that Neo Tethys was heterogeneous in terms of Os isotopes.

Appendix Table

Table A1. HSE analyses of procedural blanks and MUH-1 standard (ppb)

Sample	Os	Ir	Ru	Rh	Pt	Pd	Re	Os[1]	Re[2]	$^{187}Os/^{188}Os$
Procedural blank (n = 3)	0.007	0.001	0.001	0.007	0.018	0.084	0.017	-	-	-
MUH-1										
This study	3.445	3.429	6.619	1.085	7.188	8.905	0.197	5.204	0.191	0.1268
This study	4.989	4.179	8.049	1.158	8.225	11.300	0.159	4.292	0.192	0.1270
This study	4.191	4.105	8.830	1.124	7.938	8.363	0.182	5.696	0.189	0.1248
Average (n = 3)	4.209 ± 0.205	3.904 ± 0.068	7.833 ± 0.333	1.122 ± 0.035	7.784 ± 0.212	9.523 ± 0.267	0.180 ± 0.008	5.064	0.191	0.1262 ± 0.0016
Preferred data[2]	4.13	3.80	7.23	1.40	9.8	8.9	0.2	4.13	0.2	0.1263 ± 0.0007[3]

1 Data from montanuniversitaet leoben

2 Meisel, personal communication

3 Snortum and Day (2020)

Bibliography

Alard, O., Lorand, J.-P., Reisberg, L., Bodinier, J.-L., Dautria, J.-M., & O'reilly, S. Y. (2011). Volatile-rich metasomatism in Montferrier xenoliths (Southern France): Implications for the abundances of chalcophile and highly siderophile elements in the subcontinental mantle. *Journal of Petrology, 52*(10), 2009-2045.

Arai, S. (1994). Characterization of spinel peridotites by olivine-spinel compositional relationships: review and interpretation. *Chemical Geology, 113*(3-4), 191-204.

Aulbach, S., Mungall, J. E., & Pearson, D. G. (2016). Distribution and Processing of Highly Siderophile Elements in Cratonic Mantle Lithosphere. *Reviews in Mineralogy and Geochemistry, 81*(1), 239-304. doi:10.2138/rmg.2016.81.5

Bach, W., Garrido, C. J., Paulick, H., Harvey, J., & Rosner, M. (2004). Seawater-peridotite interactions: First insights from ODP Leg 209, MAR 15 N. *Geochemistry, Geophysics, Geosystems, 5*(9).

Ballhaus, C., Bockrath, C., Wohlgemuth-Ueberwasser, C., Laurenz, V., & Berndt, J. (2006). Fractionation of the noble metals by physical processes. *Contributions to mineralogy and petrology, 152*(6), 667-684.

Barnes, J. G. (1997). Closeness, strength, and satisfaction: examining the nature of relationships between providers of financial services and their retail customers. *Psychology & Marketing, 14*(8), 765-790.

Barnes, S.-J., Naldrett, A., & Gorton, M. (1985). The origin of the fractionation of platinum-group elements in terrestrial magmas. *Chemical Geology, 53*(3-4), 303-323.

Barnes, S. J., Mungall, J. E., & Maier, W. D. (2015). Platinum group elements in mantle melts and mantle samples. *Lithos, 232*, 395-417.

Becker, H., & Dale, C. W. (2016). Re–Pt–Os isotopic and highly siderophile element behavior in oceanic and continental mantle tectonites. *Reviews in Mineralogy and Geochemistry, 81*(1), 369-440.

Becker, H., Horan, M., Walker, R., Gao, S., Lorand, J.-P., & Rudnick, R. (2006). Highly siderophile element composition of the Earth's primitive upper mantle: constraints from new data on peridotite massifs and xenoliths. *Geochimica et Cosmochimica Acta, 70*(17), 4528-4550.

Bockrath, C., Ballhaus, C., & Holzheid, A. (2004). Fractionation of the platinum-group elements during mantle melting. *Science, 305*(5692), 1951-1953.

Bodinier, J.-L., & Godard, M. (2003). Orogenic, ophiolitic, and abyssal peridotites. *Treatise on geochemistry, 2*, 568.

Bodinier, J. (1988). Geochemistry and petrogenesis of the Lanzo peridotite body, western Alps. *Tectonophysics, 149*(1-2), 67-88.

Brenan, J., McDonough, W., & Dalpe, C. (2003). Experimental constraints on the partitioning of rhenium and some platinum-group elements between olivine and silicate melt. *Earth and Planetary Science Letters, 212*(1-2), 135-150.

Brenan, J. M. (2008a). The platinum-group elements:"Admirably adapted" for science and industry. *Elements, 4*(4), 227-232.

Brenan, J. M. (2008b). Re–Os fractionation by sulfide melt–silicate melt partitioning: a new spin. *Chemical Geology, 248*(3-4), 140-165.

Brenan, J. M., Bennett, N. R., & Zajacz, Z. (2016). Experimental results on fractionation of the highly siderophile elements (HSE) at variable pressures and temperatures during planetary and magmatic differentiation. *Reviews in Mineralogy and Geochemistry, 81*(1), 1-87.

Brenan, J. M., Finnigan, C. F., McDonough, W. F., & Homolova, V. (2012). Experimental constraints on the partitioning of Ru, Rh, Ir, Pt and Pd between chromite and silicate melt: the importance of ferric iron. *Chemical Geology, 302*, 16-32.

Brenan, J. M., McDonough, W. F., & Ash, R. (2005). An experimental study of the solubility and partitioning of iridium, osmium and gold between olivine and silicate melt. *Earth and Planetary Science Letters, 237*(3-4), 855-872.

Burton, K. W., Schiano, P., Birck, J.-L., & Allègre, C. J. (1999). Osmium isotope disequilibrium between mantle minerals in a spinel-lherzolite. *Earth and Planetary Science Letters, 172*(3-4), 311-322.

Chesley, J., Righter, K., & Ruiz, J. (2004). Large-scale mantle metasomatism: a Re–Os perspective. *Earth and Planetary Science Letters, 219*(1-2), 49-60.

Coltorti, M., Arai, S., Bonadiman, C., Faccini, B., & Ishimaru, S. (2007). Nature of metasomatizing agents in suprasubduction and intraplate settings as deduced by glass and amphibole geochemistry. *Geochimica et Cosmochimica Acta, 71*(15, Supplement), A184-A184.

Dai, J.-G., Wang, C.-S., Hébert, R., Santosh, M., Li, Y.-L., & Xu, J.-Y. (2011). Petrology and geochemistry of peridotites in the Zhongba ophiolite, Yarlung Zangbo Suture Zone: implications for the Early Cretaceous intra-oceanic subduction zone within the Neo-Tethys. *Chemical Geology, 288*(3-4), 133-148.

Day, J. M., O'Driscoll, B., Strachan, R. A., Daly, J. S., & Walker, R. J. (2017). Identification of mantle peridotite as a possible Iapetan ophiolite sliver in south Shetland, Scottish Caledonides. *Journal of the Geological Society, 174*(1), 88-92.

Defant, M. J., & Kepezhinskas, P. (2001). Evidence suggests slab melting in arc magmas.

Eos, Transactions American Geophysical Union, 82(6), 65-69.

Dick, H. J., & Bullen, T. (1984). Chromian spinel as a petrogenetic indicator in abyssal and alpine-type peridotites and spatially associated lavas. *Contributions to mineralogy and petrology, 86*(1), 54-76.

Dick, H. J., Fisher, R. L., & Bryan, W. B. (1984). Mineralogic variability of the uppermost mantle along mid-ocean ridges. *Earth and Planetary Science Letters, 69*(1), 88-106.

Dijkstra, A. H., Barth, M. G., Drury, M. R., Mason, P. R., & Vissers, R. L. (2003). Diffuse porous melt flow and melt-rock reaction in the mantle lithosphere at a slow-spreading ridge: A structural petrology and LA-ICP-MS study of the Othris Peridotite Massif (Greece). *Geochemistry, Geophysics, Geosystems, 4*(8).

Dilek, Y., & Furnes, H. (2011). Ophiolite genesis and global tectonics: Geochemical and tectonic fingerprinting of ancient oceanic lithosphere. *GSA Bulletin, 123*(3-4), 387-411. doi:10.1130/b30446.1

Dilek, Y., & Furnes, H. (2014). Ophiolites and their origins. *Elements, 10*(2), 93-100.

Eslami, A., Malvoisin, B., Grieco, G., Aradi, L. E., Marchesi, C., Cavallo, A., . . . Ikehata, K. (2021). Native copper formation associated with serpentinization in the Cheshmeh-Bid ophiolite massif (Southern Iran). *Lithos, 382*, 105953.

Fleet, M., Crocket, J., & Stone, W. (1996). Partitioning of platinum-group elements (Os, Ir, Ru, Pt, Pd) and gold between sulfide liquid and basalt melt. *Geochimica et Cosmochimica Acta, 60*(13), 2397-2412.

Fonseca, A. F. d., Herpin, U., Paula, A. M. d., Victória, R. L., & Melfi, A. J. (2007). Agricultural use of treated sewage effluents: agronomic and environmental implications and perspectives for Brazil. *Scientia Agricola, 64*, 194-209.

Fonseca, R. O., Laurenz, V., Mallmann, G., Luguet, A., Hoehne, N., & Jochum, K. P. (2012). New constraints on the genesis and long-term stability of Os-rich alloys in the Earth's mantle. *Geochimica et Cosmochimica Acta, 87*, 227-242.

Ghosh, B., & Bhatta, K. (2014). Podiform chromitites in lherzolitic mantle rocks (Andaman ophiolite, India): the role of magma/rock interaction and parental melt composition. *Bulletin de la Societe Geologique de France, 185*(2), 123-130.

Ghosh, B., Pal, T., Bhattacharya, A., & Das, D. (2009). Petrogenetic implications of ophiolitic chromite from Rutland Island, Andaman—a boninitic parentage in supra-subduction setting. *Mineralogy and Petrology, 96*(1), 59-70.

Hamlyn, P. R., Keays, R. R., Cameron, W. E., Crawford, A. J., & Waldron, H. M. (1985). Precious metals in magnesian low-Ti lavas: implications for metallogenesis and sulfur saturation in primary magmas. *Geochimica et Cosmochimica Acta, 49*(8), 1797-1811.

Harvey, J., Gannoun, A., Burton, K. W., Rogers, N. W., Alard, O., & Parkinson, I. J. (2006). Ancient melt extraction from the oceanic upper mantle revealed by Re–Os isotopes in abyssal peridotites from the Mid-Atlantic ridge. *Earth and Planetary Science Letters, 244*(3-4), 606-621.

Hassler, D. R., Peucker-Ehrenbrink, B., & Ravizza, G. E. (2000). Rapid determination of Os isotopic composition by sparging OsO4 into a magnetic-sector ICP-MS. *Chemical Geology, 166*(1-2), 1-14.

Hellebrand, E., Snow, J. E., Dick, H. J., & Hofmann, A. W. (2001). Coupled major and trace elements as indicators of the extent of melting in mid-ocean-ridge peridotites. *Nature, 410*(6829), 677-681.

Jagoutz, E., Palme, H., Baddenhausen, H., Blum, K., Cendales, M., Dreibus, G., . . . Wänke, H. (1979). *The abundances of major, minor and trace elements in the earth's mantle as derived from primitive ultramafic nodules.* Paper presented at the In: Lunar and Planetary Science Conference, 10th, Houston, Tex., March 19-23, 1979, Proceedings. Volume 2.(A80-23617 08-91) New York, Pergamon Press, Inc., 1979, p. 2031-2050. Research supported by the Deutsche Forschungsgemeinschaft.

Jaques, A., & Green, D. (1980). Anhydrous melting of peridotite at 0–15 kb pressure and the genesis of tholeiitic basalts. *Contributions to mineralogy and petrology, 73*, 287-310.

Johnson, K. T., Dick, H. J., & Shimizu, N. (1990). Melting in the oceanic upper mantle: an ion microprobe study of diopsides in abyssal peridotites. *Journal of Geophysical Research: Solid Earth, 95*(B3), 2661-2678.

Kepezhinskas, P., Defant, M. J., & Widom, E. (2002). Abundance and distribution of PGE and Au in the island-arc mantle: implications for sub-arc metasomatism. *Lithos, 60*(3-4), 113-128.

Klein, F., & Bach, W. (2009). Fe–Ni–Co–O–S phase relations in peridotite–seawater interactions. *Journal of Petrology, 50*(1), 37-59.

Klein, F., Bach, W., & McCollom, T. M. (2013). Compositional controls on hydrogen generation during serpentinization of ultramafic rocks. *Lithos, 178*, 55-69.

Leake, B. E., Woolley, A. R., Arps, C. E., Birch, W. D., Gilbert, M. C., Grice, J. D., . . . Krivovichev, V. G. (1997). Nomenclature of amphiboles; report of the subcommittee on amphiboles of the International Mineralogical Association, Commission on New Minerals and Mineral Names. *The Canadian Mineralogist, 35*(1), 219-246.

Levasseur, S., Birck, J.-L., & Allègre, C. J. (1998). Direct measurement of femtomoles of osmium and the 187Os/186Os ratio in seawater. *Science, 282*(5387), 272-274.

Liu, C.-Z., Chung, S.-L., Wu, F.-Y., Zhang, C., Xu, Y., Wang, J.-G., . . . Guo, S. (2016).

Tethyan suturing in Southeast Asia: Zircon U-Pb and Hf-O isotopic constraints from Myanmar ophiolites. *Geology, 44*(4), 311-314.

Liu, C.-Z., Snow, J. E., Brügmann, G., Hellebrand, E., & Hofmann, A. W. (2009). Non-chondritic HSE budget in Earth's upper mantle evidenced by abyssal peridotites from Gakkel ridge (Arctic Ocean). *Earth and Planetary Science Letters, 283*(1-4), 122-132.

Liu, C.-Z., Snow, J. E., Hellebrand, E., Brügmann, G., Von Der Handt, A., Büchl, A., & Hofmann, A. W. (2008). Ancient, highly heterogeneous mantle beneath Gakkel ridge, Arctic Ocean. *Nature, 452*(7185), 311-316.

Liu, C.-Z., Wu, F.-Y., Chu, Z.-Y., Ji, W.-Q., Yu, L.-J., & Li, J.-L. (2012). Preservation of ancient Os isotope signatures in the Yungbwa ophiolite (southwestern Tibet) after subduction modification. *Journal of Asian Earth Sciences, 53*, 38-50.

Liu, C.-Z., Zhang, C., Xu, Y., Wang, J.-G., Chen, Y., Guo, S., . . . Sein, K. (2016). Petrology and geochemistry of mantle peridotites from the Kalaymyo and Myitkyina ophiolites (Myanmar): Implications for tectonic settings. *Lithos, 264*, 495-508.

Liu, J., Rudnick, R. L., Walker, R. J., Gao, S., Wu, F., & Piccoli, P. M. (2010). Processes controlling highly siderophile element fractionations in xenolithic peridotites and their influence on Os isotopes. *Earth and Planetary Science Letters, 297*(1-2), 287-297.

Lorand, J.-P., Alard, O., & Luguet, A. (2010). Platinum-group element micronuggets and refertilization process in Lherz orogenic peridotite (northeastern Pyrenees, France). *Earth and Planetary Science Letters, 289*(1-2), 298-310.

Lorand, J.-P., Alard, O., Luguet, A., & Keays, R. R. (2003). Sulfur and selenium systematics of the subcontinental lithospheric mantle: inferences from the Massif Central xenolith suite (France). *Geochimica et Cosmochimica Acta, 67*(21), 4137-4151.

Lorand, J.-P., Delpech, G., Grégoire, M., Moine, B., O'Reilly, S. Y., & Cottin, J.-Y. (2004). Platinum-group elements and the multistage metasomatic history of Kerguelen lithospheric mantle (South Indian Ocean). *Chemical Geology, 208*(1-4), 195-215.

Lorand, J.-P., Luguet, A., & Alard, O. (2013). Platinum-group element systematics and petrogenetic processing of the continental upper mantle: A review. *Lithos, 164*, 2-21.

Luguet, A., Lorand, J.-P., & Seyler, M. (2003). Sulfide petrology and highly siderophile element geochemistry of abyssal peridotites: A coupled study of samples from the Kane Fracture Zone (45 W 23 20N, MARK area, Atlantic Ocean). *Geochimica et Cosmochimica Acta, 67*(8), 1553-1570.

Luguet, A., Nowell, G. M., & Pearson, D. G. (2008). 184Os/188Os and 186Os/188Os

measurements by Negative Thermal Ionisation Mass Spectrometry (N-TIMS): effects of interfering element and mass fractionation corrections on data accuracy and precision. *Chemical Geology, 248*(3-4), 342-362.

Luguet, A., & Reisberg, L. (2016). Highly siderophile element and 187Os signatures in non-cratonic basalt-hosted peridotite xenoliths: Unravelling the origin and evolution of the post-Archean lithospheric mantle. *Reviews in Mineralogy and Geochemistry, 81*(1), 305-367.

Luguet, A., Shirey, S. B., Lorand, J.-P., Horan, M. F., & Carlson, R. W. (2007). Residual platinum-group minerals from highly depleted harzburgites of the Lherz massif (France) and their role in HSE fractionation of the mantle. *Geochimica et Cosmochimica Acta, 71*(12), 3082-3097.

Mallmann, G., & O'Neill, H. S. C. (2007). The effect of oxygen fugacity on the partitioning of Re between crystals and silicate melt during mantle melting. *Geochimica et Cosmochimica Acta, 71*(11), 2837-2857.

Malvoisin, B. (2015). Mass transfer in the oceanic lithosphere: serpentinization is not isochemical. *Earth and Planetary Science Letters, 430*, 75-85.

Mansur, E. T., Barnes, S.-J., & Duran, C. J. (2021). An overview of chalcophile element contents of pyrrhotite, pentlandite, chalcopyrite, and pyrite from magmatic Ni-Cu-PGE sulfide deposits. *Mineralium Deposita, 56*, 179-204.

Marchesi, C., Garrido, C. J., Harvey, J., González-Jiménez, J. M., Hidas, K., Lorand, J.-P., & Gervilla, F. (2013). Platinum-group elements, S, Se and Cu in highly depleted abyssal peridotites from the Mid-Atlantic Ocean Ridge (ODP Hole 1274A): influence of hydrothermal and magmatic processes. *Contributions to mineralogy and petrology, 166*(5), 1521-1538.

Mavrogenes, J. A., & O'Neill, H. S. C. (1999). The relative effects of pressure, temperature and oxygen fugacity on the solubility of sulfide in mafic magmas. *Geochimica et Cosmochimica Acta, 63*(7-8), 1173-1180.

McDonough, W. F., & Sun, S.-S. (1995). The composition of the Earth. *Chemical Geology, 120*(3-4), 223-253.

Meisel, T., Walker, R. J., Irving, A. J., & Lorand, J.-P. (2001). Osmium isotopic compositions of mantle xenoliths: a global perspective. *Geochimica et Cosmochimica Acta, 65*(8), 1311-1323.

Mitchell, R. H., & Keays, R. R. (1981). Abundance and distribution of gold, palladium and iridium in some spinel and garnet lherzolites: implications for the nature and origin of precious metal-rich intergranular components in the upper mantle. *Geochimica et Cosmochimica Acta, 45*(12), 2425-2442.

Mungall, J. E., Andrews, D. R., Cabri, L. J., Sylvester, P. J., & Tubrett, M. (2005). Partitioning of Cu, Ni, Au, and platinum-group elements between monosulfide solid solution and sulfide melt under controlled oxygen and sulfur fugacities. *Geochimica et Cosmochimica Acta, 69*(17), 4349-4360.

Mungall, J. E., & Brenan, J. M. (2014). Partitioning of platinum-group elements and Au between sulfide liquid and basalt and the origins of mantle-crust fractionation of the chalcophile elements. *Geochimica et Cosmochimica Acta, 125*, 265-289.

Niu, X., Liu, F., Yang, J., Dilek, Y., Xu, Z., & Sein, K. (2018). Mineralogy, geochemistry, and melt evolution of the Kalaymyo peridotite massif in the Indo-Myanmar Ranges (western Myanmar), and tectonic implications. *Lithosphere, 10*(1), 79-94.

Niu, X., Yang, J., Dilek, Y., Xu, J., Li, J., Chen, S., . . . Liu, Z. (2015). Petrological and Os isotopic constraints on the origin of the Dongbo peridotite massif, Yarlung Zangbo Suture Zone, Western Tibet. *Journal of Asian Earth Sciences, 110*, 72-84.

Niu, Y. (1997). Mantle melting and melt extraction processes beneath ocean ridges: evidence from abyssal peridotites. *Journal of Petrology, 38*(8), 1047-1074.

Niu, Y. (2004). Bulk-rock major and trace element compositions of abyssal peridotites: implications for mantle melting, melt extraction and post-melting processes beneath mid-ocean ridges. *Journal of Petrology, 45*(12), 2423-2458.

O'Neill, H. S. C. (1991). The origin of the Moon and the early history of the Earth—A chemical model. Part 2: The Earth. *Geochimica et Cosmochimica Acta, 55*(4), 1159-1172.

O'Driscoll, B., & González-Jiménez, J. M. (2016). Petrogenesis of the platinum-group minerals. *Reviews in Mineralogy and Geochemistry, 81*(1), 489-578.

Pan, Q.-Q., Xiao, Y., Su, B.-X., Liu, X., Robinson, P. T., Uysal, I., . . . Sakyi, P. A. (2022). Amphibole as a witness of chromitite formation and fluid metasomatism in ophiolites. *American Mineralogist: Journal of Earth and Planetary Materials, 107*(2), 294-305.

Park, G., Park, J.-W., Heo, C.-H., & Kim, J. (2022). Distribution of mantle-melt interaction zone: A petrological exploration tool for podiform chromitite deposits in the Kalaymyo ophiolite, Myanmar. *Journal of Geochemical Exploration, 232*, 106878.

Park, J.-W., Campbell, I. H., & Eggins, S. M. (2012). Enrichment of Rh, Ru, Ir and Os in Cr spinels from oxidized magmas: Evidence from the Ambae volcano, Vanuatu. *Geochimica et Cosmochimica Acta, 78*, 28-50.

Park, J.-W., Park, G., Heo, C.-H., & Kim, J. (2017). A Geochemical indicator in exploration for the Kalaymyo chromitite deposit, Myanmar. *Economic and Environmental Geology, 50*(6), 423-433.

Parkinson, I. J., & Pearce, J. A. (1998). Peridotites from the Izu–Bonin–Mariana forearc (ODP Leg 125): evidence for mantle melting and melt–mantle interaction in a supra-subduction zone setting. *Journal of Petrology, 39*(9), 1577-1618.

Paton, C., Hellstrom, J., Paul, B., Woodhead, J., & Hergt, J. (2011). Iolite: Freeware for the visualisation and processing of mass spectrometric data. *Journal of Analytical Atomic Spectrometry, 26*(12), 2508-2518.

Paulick, H., Bach, W., Godard, M., De Hoog, J., Suhr, G., & Harvey, J. (2006). Geochemistry of abyssal peridotites (Mid-Atlantic Ridge, 15 20′ N, ODP Leg 209): implications for fluid/rock interaction in slow spreading environments. *Chemical Geology, 234*(3-4), 179-210.

Pearce, J. A., Barker, P., Edwards, S., Parkinson, I. J., & Leat, P. (2000). Geochemistry and tectonic significance of peridotites from the South Sandwich arc–basin system, South Atlantic. *Contributions to mineralogy and petrology, 139*(1), 36-53.

Pearson, D., Irvine, G., Ionov, D., Boyd, F., & Dreibus, G. (2004). Re–Os isotope systematics and platinum group element fractionation during mantle melt extraction: a study of massif and xenolith peridotite suites. *Chemical Geology, 208*(1-4), 29-59.

Peregoedova, A., Barnes, S.-J., & Baker, D. R. (2004). The formation of Pt–Ir alloys and Cu–Pd-rich sulfide melts by partial desulfurization of Fe–Ni–Cu sulfides: results of experiments and implications for natural systems. *Chemical Geology, 208*(1-4), 247-264.

Rehkaemper, M., Halliday, A., Fitton, J., Lee, D.-C., Wieneke, M., & Arndt, N. (1999). Ir, Ru, Pt, and Pd in basalts and komatiites: new constraints for the geochemical behavior of the platinum-group elements in the mantle. *Geochimica et Cosmochimica Acta, 63*(22), 3915-3934.

Reisberg, L. (2021). Osmium isotope constraints on formation and refertilization of the non-cratonic continental mantle lithosphere. *Chemical Geology, 574*, 120245.

Robinson, P. T., Zhou, M.-F., Malpas, J., & Bai, W.-J. (1997). Podiform chromitites: their composition, origin and environment of formation. *Episodes Journal of International Geoscience, 20*(4), 247-252.

Rudnick, R. L., & Walker, R. J. (2009). Interpreting ages from Re–Os isotopes in peridotites. *Lithos, 112*, 1083-1095.

Saunders, A. D., & Tarney, J. (1979). The geochemistry of basalts from a back-arc spreading centre in the East Scotia Sea. *Geochimica et Cosmochimica Acta, 43*(4), 555-572.

Schulte, R. F., Schilling, M., Anma, R., Farquhar, J., Horan, M. F., Komiya, T., . . . Walker, R. J. (2009). Chemical and chronologic complexity in the convecting upper mantle: Evidence from the Taitao ophiolite, southern Chile. *Geochimica et Cosmochimica*

Acta, 73(19), 5793-5819.

Schwarzenbach, E. M., Vrijmoed, J. C., Engelmann, J. M., Liesegang, M., Wiechert, U., Rohne, R., & Plümper, O. (2021). Sulfide dissolution and awaruite formation in continental serpentinization environments and its implications to supporting life. *Journal of Geophysical Research: Solid Earth, 126*(5), e2021JB021758.

Sharma, M., Papanastassiou, D., & Wasserburg, G. (1997). The concentration and isotopic composition of osmium in the oceans. *Geochimica et Cosmochimica Acta, 61*(16), 3287-3299.

Shirey, S. B., & Walker, R. J. (1998). The Re-Os isotope system in cosmochemistry and high-temperature geochemistry. *Annual review of earth and planetary sciences, 26*(1), 423-500.

Singh, A. K. (2013). Petrology and geochemistry of Abyssal Peridotites from the Manipur Ophiolite Complex, Indo-Myanmar Orogenic Belt, Northeast India: Implication for melt generation in mid-oceanic ridge environment. *Journal of Asian Earth Sciences, 66*, 258-276.

Snortum, E., & Day, J. M. (2020). Forearc origin for Coast Range Ophiolites inferred from osmium isotopes and highly siderophile elements. *Chemical Geology, 550*, 119723.

Snow, J. E., & Dick, H. J. (1995). Pervasive magnesium loss by marine weathering of peridotite. *Geochimica et Cosmochimica Acta, 59*(20), 4219-4235.

Snow, J. E., & Reisberg, L. (1995). Os isotopic systematics of the MORB mantle: results from altered abyssal peridotites. *Earth and Planetary Science Letters, 133*(3-4), 411-421.

Snow, J. E., & Schmidt, G. (1998). Constraints on Earth accretion deduced from noble metals in the oceanic mantle. *Nature, 391*(6663), 166-169.

Standish, J., Hart, S., Blusztajn, J., Dick, H., & Lee, K. (2002). Abyssal peridotite osmium isotopic compositions from cr-spinel. *Geochemistry, Geophysics, Geosystems, 3*(1), 1-24.

Till, C. B., Grove, T. L., & Withers, A. C. (2012). The beginnings of hydrous mantle wedge melting. *Contributions to mineralogy and petrology, 163*(4), 669-688.

Walker, R., Carlson, R., Shirey, S., & Boyd, F. (1989). Os, Sr, Nd, and Pb isotope systematics of southern African peridotite xenoliths: implications for the chemical evolution of subcontinental mantle. *Geochimica et Cosmochimica Acta, 53*(7), 1583-1595.

Wang, J., Xiong, X., Chen, Y., & Huang, F. (2020). Redox processes in subduction zones: Progress and prospect. *Science China Earth Sciences, 63*, 1952-1968.

Watson, E. B., Othman, D. B., Luck, J.-M., & Hofmann, A. W. (1987). Partitioning of U, Pb, Cs, Yb, Hf, Re and Os between chromian diopsidic pyroxene and haplobasaltic

liquid. *Chemical Geology, 62*(3-4), 191-208.

Woodland, S., Pearson, D., & Thirlwall, M. (2002). A platinum group element and Re–Os isotope investigation of siderophile element recycling in subduction zones: comparison of Grenada, Lesser Antilles Arc, and the Izu–Bonin Arc. *Journal of Petrology, 43*(1), 171-198.

Xu, Y., Li, D., Li, D., Dong, G. C., Pearson, D. G., & Liu, J. (2021). Modification of lithospheric mantle by melts/fluids with different sulfur fugacities during the Wilson cycle: insights from Lesvos and global ophiolitic peridotites. *Journal of Geophysical Research: Solid Earth, 126*(8), e2021JB022445.

Xu, Y., & Liu, C.-Z. (2019). Subduction-induced fractionated highly siderophile element patterns in forearc mantle. *Minerals, 9*(6), 339.

Xu, Y., Liu, J., Xiong, Q., Su, B.-X., Scott, J. M., Xu, B., . . . Pearson, D. G. (2020). The complex life cycle of oceanic lithosphere: A study of Yarlung-Zangbo ophiolitic peridotites, Tibet. *Geochimica et Cosmochimica Acta, 277*, 175-191.

Yang, T. N., Hou, Z. Q., Wang, Y., Zhang, H. R., & Wang, Z. L. (2012). Late Paleozoic to Early Mesozoic tectonic evolution of northeast Tibet: Evidence from the Triassic composite western Jinsha-Garzê-Litang suture. *Tectonics, 31*(4).

Zhang, M., & Li, Y. (2021). Breaking of Henry's law for sulfide liquid–basaltic melt partitioning of Pt and Pd. *Nature Communications, 12*(1), 5994.

Zhang, Z., & Hirschmann, M. M. (2016). Experimental constraints on mantle sulfide melting up to 8 GPa. *American Mineralogist, 101*(1), 181-192.

Zhou, M.-F., & Robinson, P. T. (1997). Origin and tectonic environment of podiform chromite deposits. *Economic Geology, 92*(2), 259-262.

Zindler, A., & Hart, S. (1986). Chemical geodynamics. *Annual review of earth and planetary sciences, 14*, 493-571.

박정우, 박규승, 허철호, & 김지혁. (2017). 미얀마 깔레이미요 크롬철석광상 탐사의 지구화학적 인자. *자원환경지질, 50*(6), 423-433.

국문 초록

부분용융과 용융체-암석 반응이 상부 맨틀의 친철성 원소에 미치는 영향은 아직 잘 알려지지 않았다. 본 연구에서는 깔레이미요 오피올라이트 하즈버가이트를 통해 맨틀 부분용융과 용융체-암석 반응의 과정에서 친철성 원소 및 오스뮴 동위원소의 지구화학적 거동을 연구했다. 기존 연구결과에 따르면 이 하즈버가이트는 암석학적 및 지구화학적 특징에 따라 두개의 그룹으로 구분된다. 그룹1 하즈버가이트는 낮은 정도의 부분용융을 겪은 잔여 맨틀의 감람암을 대표하며 낮은 첨정석 Cr#와 높은 전암 Al_2O_3및 CaO 함량을 함유한다. 반면, 그룹2 하즈버가이트는 더 높은 정도의 부분용융을 대표하며, 그룹1에 비해 높은 첨정석 Cr#와 낮은 전암 Al_2O_3 및 CaO 함량 함유한다. 또한, 그룹 2 하즈버가이트는 다양한 맨틀-용융체 상호반응 조직이 관찰되며 높은 TiO_2 함유량의 첨정석 갖는다. 그러므로 깔레이미요 오피올라이트는 부분용융과 맨틀-용융체 상호반응에 따른 친동성원소 거동을 연구하기에 적합한 시료이다.

전암 친철성 원소 함량을 분석한 결과, 친철성 원소 함량은 사문화의 영향을 받지 않은 것으로 확인된다. 이리듐 그룹 백금족원소(IPGE)함량은 두 그룹에서 부분용융 정도가 증가함에 따라 증가하는 경향이 관찰됐다. 준 분별 용융 모델에 따르면 부분용융이 진행되어 황화물이 소진된 이후에는 규산염광물인 감람석 또한 IPGE

함량을 주로 함유할 수 있는 것으로 해석된다. 또한, 중복 분석 간의 차이가 있던 시료는 고도로 결핍된 감람암에서 합금 또한 IPGE 함량을 크게 조절함을 의미하며, IPGE 합금을 통해 확인된다. 팔라듐 그룹 백금족원소(PPGE) 함량은 그룹1에서 부분용융 정도가 증가함에도 유지 혹은 감소되는 반면 그룹2에서는 중복 분석 간의 큰 차이와 함께 넓은 범위에 분포한다. PPGE의 부분용융 모델은 IPGE보다 낮은 3000의 분배계수에서 PPGE의 함량을 가장 잘 설명하며, 이는 최근 보고된 실험 연구의 결과에 부합한다. PPGE 용융 모델은 규산염광물에 대한 분배계수를 고려한 것과 하지 않은 모델에 큰 차이가 없으며, 이는 PPGE 함량이 규산염광물에 영향을 유의미하게 받지 않음을 의미한다. 일차 황화물은 그룹2 하즈버가이트에서 대부분 소진되며 용융모델의 Pd/Ir은 이와 함께 급감한다. 그룹2의 넓은 PPGE 함량 범위 및 용융에 따른 낮은 예상 값에 비해 높은 Pd/Ir은 다양한 정도의 맨틀-용융체 상호반응을 통한 이차황화물의 유입의 결과이며, 황화물 침전 모델 및 각섬석과 연계된 이차 황화물 및 백금의 산출로 확인된다. 섭입대 용융체의 높은 산화도로 인해 황화물이 유입되었음에도 Re은 유입되지 못했으며, 이에 따라 변화하지 않은 오스뮴 동위원소는 신-데티스해가 오스뮴 동위원소의 측면에서 불균질함을 의미한다.

Keyword: 친철성 원소, 부분용융, 맨틀-용융체 상호작용

Student Number: 2021-28917